Geophysical Journal International

Geophys. J. Int. (2021) **226,** 2073–2102
Advance Access publication 2021 May 14
GJI Marine Geosciences and Applied Geophysics

https://doi.org/10.1093/gji/ggab194

The crustal structure of the Kerimbas Basin across the offshore branch of the East African Rift System

Maren Vormann[1] and Wilfried Jokat[1,2]

[1] *Alfred Wegener Institute, Helmholtz Centre for Polar and Marine Research, Am Handelshafen* 12, 27570 *Bremerhaven, Germany*
[2] *Department of Geosciences, University of Bremen, Klagenfurter Strasse* 4, 28359 *Bremen, Germany. E-mail: Wilfried.Jokat@awi.de*

Accepted 2021 May 12. Received 2021 May 7; in original form 2021 January 19

SUMMARY

The Davie Fracture Zone (DFZ) evolved during the Jurassic and Cretaceous breakup and subsequent drift of Gondwana off East Africa. This old weak zone has been reactivated during the evolution of the East African Rift System. Recent faulting of Cenozoic sediments in the Kerimbas Basin off northern Mozambique shows that they are affected by the neotectonics. The question is if and how the crustal fabric in our research area has been modified by the rifting process. We present two seismic refraction profiles acquired offshore northern Mozambique to investigate its regional crustal structure and tectonic history. The profiles show a continent–ocean transition zone that widens from around 40 km at 13°S to more than 100 km at 11°S. In the west the transitional crust is up to 12 km thick. To the east, around 150 km off the Mozambique coast lies oceanic crust whose thickness varies from 4.9 to 6.5 km along the northern line and from 6.5 to 7.5 km along the southern one. The latter presents an unusual high-velocity lower crustal body (7.0–7.2 km s^{-1}), about 40 km wide and 3.8 km thick, underlying the oceanic crust. The body may consist of underplated melt with the same source as the nearby Paisley Seamount, which has not yet reached its isostatic equilibrium. Despite well documented recent seismicity along the margin, neither of the profiles reveal significant crustal modifications or reduced crustal seismic velocities that might be related to ongoing extensional tectonics as part of of the East African Rift System. Neither profile reveals seismic evidence for the presence of a major fracture zone or sheared continental margin parallel to the margin. Instead, the profiles' broad continent–ocean transitions are consistent with their formation during an early Jurassic stage of plate divergence oblique to the margin. Later, after 157 Ma, the azimuth of relative plate motion between East and West Gondwana changed to be parallel to the margin, and parts of the continent–ocean transitions may have been locally reactivated in a strike-slip sense. However, details on the plate movements during the directional change of the seafloor spreading between 157 and 144 Ma are not available. The oceanic crust formed by the initial divergent oblique extension became faulted/modified by the strike-slip movements between both plates. Instead of a narrow deformation zone, the DFZ is charcaterized by a broad, diffuse zone of transtensional deformation.

Key words: Indian Ocean; Controlled source seismology; Continental margins: transform; Crustal structure; Neotectonics; Transform faults.

1 INTRODUCTION

One of the world's oldest oceanic basins, the Jurassic West Somali Basin, is located between East Africa, Madagascar, and India, where it formed during the breakup of Gondwana (rifting started around 182 Ma) (König & Jokat 2006; Müller & Jokat 2019). The two basins lie off NE-striking segments of the East African continental margin, and are connected by a north-trending segment that runs parallel to the continental margin of northern Mozambique and Tanzania. Offshore of this segment, a complex of elongated basement ridges and basins known as the Davie Fracture Zone (DFZ) hosts the palaeo-plate boundary (Fig. 1). The timing and kinematics of the East Gondwana-West Gondwana breakup are discussed in several studies (Lawver *et al.* 1991; Cox 1992; Jokat *et al.* 2003; König & Jokat 2006; Eagles & König 2008; Leinweber & Jokat 2012; Reeves 2014; Phethean *et al.* 2016; Müller & Jokat 2017; Tuck-Martin *et al.* 2018; Müller & Jokat 2019; Thompson *et al.* 2019). Because of sparse data coverage, only a limited number of studies

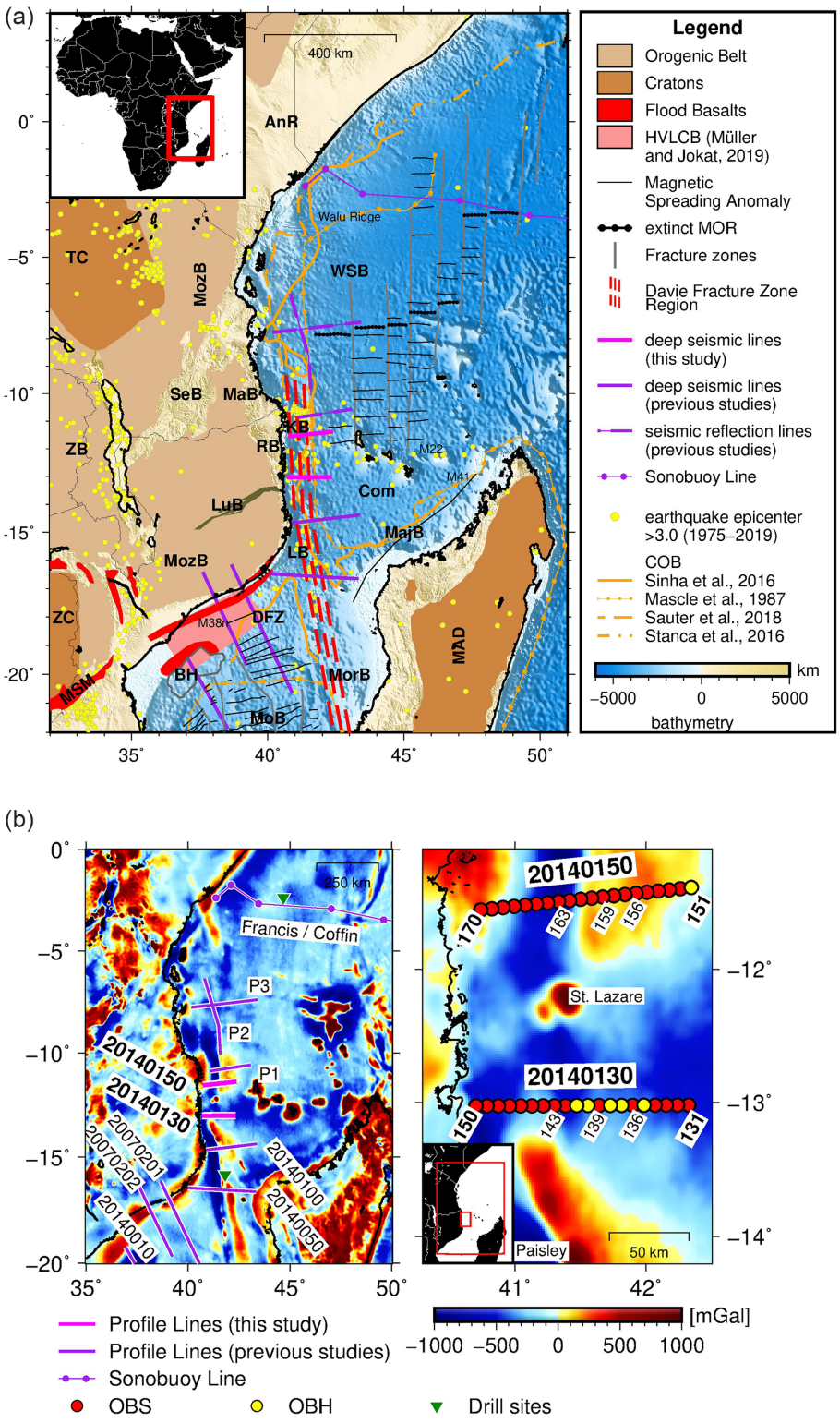

Figure 1. (a) Overview of the main geologic features, fracture zones, magmatic intrusions and magmatic chrons in the Somali Basin, Mozambique Channel, Mozambique Basin and eastern Africa. Lines from previous studies are taken from Leinweber et al. (2013), Müller et al. (2016), Müller & Jokat (2017), Sinha et al. (2019) and Vormann et al. (2020). The bathymetry is taken from GEBCO (2014). The terranes, flood basalts and fracture zones are digitized after Müller et al. (2016). Abbreviations: AnR, Anza Rift; BH, Beira High; Com, Comores islands; DFZ, Davie Fracture Zone; KB, Kerimbas Basin; LB, Lacerda Basin; LuB, Lurio Belt; MAD, Madagascar; MajB, Majunga Basin; MoB, Mozambique Basin; MorB, Morandava Basin; MozB, Mozambique Belt; MSM, Monokline Sabi Monokline; RB, Rovuma Basin; SeB, Selous Basin; TC, Tanzania Craton; WSB, West Somali Basin; ZB, Zambesi Belt; ZC, Zambesi Craton. (b) Overview of the position of the seismic refraction lines in our study with gravity data as background information (left); and enlarged part (right) focussing on our research area. The distribution of ocean bottom seismometers (OBS, red) and ocean bottom hydrophones (OBH, yellow) along both profiles is indicated. The gravity data are taken from Sandwell *et al.* (2014).

(Davis *et al.* 2016; Phethean *et al.* 2016; Sauter *et al.* 2016, 2018; Sinha *et al.* 2019) focus on the West Somali Basin. The best constraints for the timing and drift direction of both plates come from the Mozambique Basin. There, the first oceanic crust was formed at chron M38n.2n (164.1 Ma; Müller & Jokat, 2017, 2019). As seen from Africa, most kinematic reconstructions indicate that the initial drift direction was NW–SE perpendicular to the Central Mozambican margin but oblique to the margins of northern Mozambique and Tanzania (e.g. Reeves 2014; Davis *et al.* 2016; Phethean *et al.* 2016; Tuck-Martin *et al.* 2018; Müller & Jokat 2019). Later, between chron M26r (157 Ma) and chron M18n (144 Ma) the relative plate motion changed to a nearly north–south orientation (Fig. 2). These motions imply a history of oblique plate divergence followed by a transform motion along the DFZ that can be expected to have given rise to its present-day appearance (Vormann *et al.* 2020).

The earliest offshore geophysical investigations of the West Somali Basin, the DFZ, and the Mozambique Channel took place during the 70s and 80s by US/French expeditions (Francis *et al.* 1966; Bunce *et al.*, 1967; Heirtzler & Burroughs 1971; Scrutton 1978; Lort *et al.* 1979; Scrutton *et al.* 1981; Coffin *et al.* 1986; Mougenot *et al.* 1986a; Coffin & Rabinowitz 1987; Virlogeux 1987; Leclaire *et al.* 1989; Stanca *et al.*, 2016). These expeditions returned evidence for a complex crustal fabric of the DFZ, but also for active faulting off northern Mozambique. Scientific seismic reflection experiments off northern Mozambique were resumed only in the last decade, with the aim to describe the regional sedimentation history and crustal structure (Franke *et al.* 2015; Klimke & Franke 2016; Klimke *et al.* 2016, 2018; Sauter *et al.* 2016, 2018; Sinha *et al.* 2019). In general they confirmed observations of earlier studies.

Seismological studies of the region have identified the DFZ as a focus of ongoing seismicity, and interpreted it as a zone of intraplate crustal weakness (Stamps *et al.* 2008; Déprez *et al.* 2013; Mulibo & Nyblade 2016; Stamps *et al.* 2018). This region is experiencing reactivation within the same regional stress field as that responsible for ongoing rifting of Eastern Africa. Two elongated seafloor depressions, the Kerimbas and Lacerda basins, overlie the DFZ basement and are related to faulting in this stress field since Miocene times (Franke *et al.* 2015). As such, the area off Tanzania and Northern Mozambique represents an offshore branch of the East African Rift System (EARS; Mougenot *et al.* 1986a; Chorowicz 2005). The EARS is understood to host a number of small plates, which diverge along an approximate E–W orientation at rates of ∼2.7 to 1.2 mm yr^{-1} (Stamps *et al.* 2008; Saria *et al.* 2014). The reactivated DFZ is considered to be the plate boundary between the so-called Rovuma and Lwandle microplates (Stamps *et al.* 2018).

Despite the plate kinematic evidence for a complex early rifting history, and seismic and seismological evidence for renewed Neogene to present rifting in the DFZ region, the crustal fabric off Northern Mozambique is currently unknown. To rectify this, we use deep seismic sounding data collected in 2014 by the MOCOM and PAGE-Four RV Sonne cruises SO-230 and SO-231 in the southern West Somali Basin, offshore Northern Mozambique. In this study, we present our seismic amplitude and 2.5D gravity modelling of two seismic refraction profiles over the basin, and our interpretations of the results. The improved knowledge of the crustal structure of the Mozambique Channel and southern West Somali Basin strengthen kinematic models for the early breakup of Gondwana and provide insights into the extent of modification of oceanic crust by reactivation of ancient fracture zones in an extensional stress field.

2 GEOLOGIC SETTING

Large sedimentary basins characterize the northern Mozambican and Tanzanian continental margins. Onshore, the Rovuma Basin (Fig. 1a) strikes N–S between Nacala and southern Tanzania. It has a maximum onshore E–W extent of 160 km with a sedimentary fill up to 10 km thick (Key *et al.* 2008). The onshore parts of the Rovuma Basin are underlain by crystalline and metaphoric basement rocks, and formed by Mesozoic crustal extension (Salman & Abdula 1995). The oldest marine sediments in the offshore Rovuma Basin, near the Pemba Formation, are dated to Late Jurassic age (Smelror *et al.* 2008). The Mandawa and Selous basins lie further north in Tanzania (Wopfner & Kaaya 1991; Veeken & Titov 1996). On the opposing side of the Mozambique Channel, northern and western Madagascar and its continental shelf host the major sedimentary Morondava and Majunga basins (Geiger *et al.* 2004). The Comoros islands in the Comoros Basin off northern Madagascar (Fig. 1a) are attributed to Neogene and recent volcanism (Emerick & Duncan 1982).

The oldest tectonic units bordering the Mozambique Channel are the Archean cratons of Madagascar, Zambesi, and Tanzania (Fig. 1a). The Lurio Belt in central Mozambique is a long–lived polyphase shear zone created during the Kiberian orogeny, which led to the assembly of Rodinia in the Mesoproterozoic (Grantham *et al.* 2003; Ueda *et al.* 2012). The Lurio Belt is surrounded by the Mozambique Belt, which developed later during the Pan-African orogeny that led to the assembly of Gondwana in Neoproterozoic and early Phanerozoic times (Grantham *et al.* 2003, Sacchi *et al.* 2000).

In the Mozambique Channel, the Davie Ridge (DR) is defined as the topographic expression of the DFZ (Bunce & Molnar 1977; Fig. 1). The DR was discovered in 1970 during the oceanographic cruise CH99 of RV *Chain* (Bassias 1992). It is flanked to the west by the Kerimbas and Lacerda basins (Fig. 1a). The DR stretches between 5°S and 20°S and can be divided into two segments on the basis of topographic changes at 13°S (Fig. 1a).

The southern segment (13°–20°S) hosts four large volcanic seamounts: St. Lazare, Paisley, Macua and Sakalaves seamounts (Fig. 1a). The southern DR rises up from 2700 to 300 m below sea level (Mougenot *et al.* 1986a). Mahanjane (2014) proposes that the seamounts could be products of recent volcanism, probably related to the ongoing crustal extension as the EARS. Based on dredged rock samples, Bassias (1992) suggests that the southern part of DR is composed of crystalline continental basement (granites, gneisses and meta-arkoses). LeClaire *et al.* (1989) note similarities in the compositions of rocks from the DR and those of the Karoo sequences found in Tanzania and Madagascar. Vormann et al (2020) suggested that compressional forces acting during the formation of the young DFZ might have caused the uplift of the continental crust beneath the DR. On the southernmost Sakalaves seamount, Courgeon *et al.* (2018) found evidence for recent volcanic activity.

The DR vanishes at 13°S, where it intersects the offshore projection of the Lurio Belt. It reappears further north (5°S to 13°S) as a ridge that rises up by about 1000 m above the surrounding seafloor to 1700 m below sea level (Mougenot *et al.* 1986a). The northern DR is asymmetrical, with a steep western flank that also forms the eastern margin of the Kerimbas Basin (Mougenot *et al.* 1986a). The northern DR was dredged during the RIDA/M39 cruise (LeClaire *et al.* 1989; Mougenot *et al.* 1986b; Virlogeux

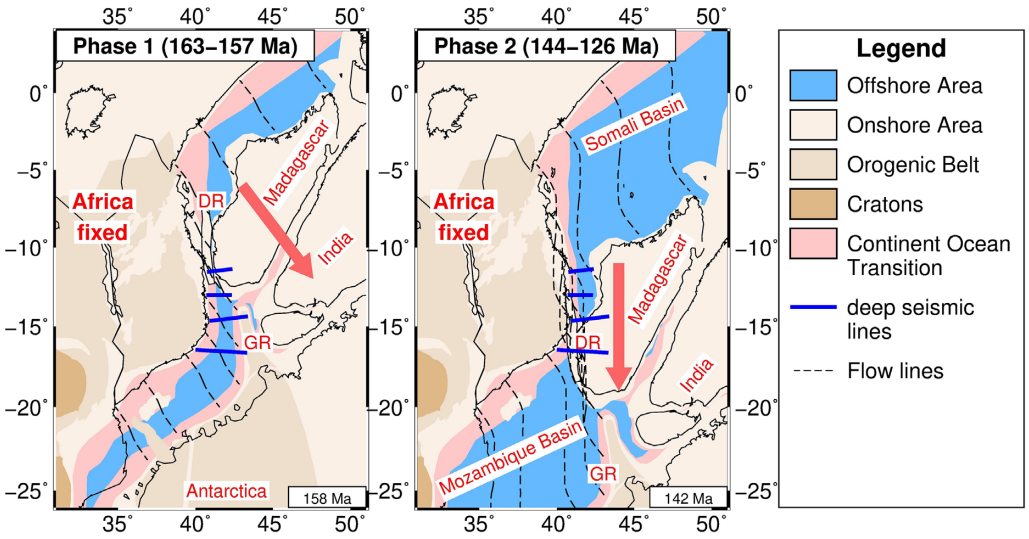

Figure 2. Two phase model of the initial movements between East and West Gondwana (Müller and Jokat 2019) to indicate the plate movements for the time period relevant for our study. Red arrows mark the direction of East Gondwana (Antarctica, India, Madagascar) plate movements relative to West Gondwana (Africa).

1987) and the recovered rocks were identified as possible mylonites (Virlogeux 1987).

The Kerimbas Basin is a prominent graben structure located between 13° and 10°S running parallel to the northern DR on its western flank. At the seafloor, the graben is 30 km wide and about 150 km long and shows signs of post-Miocene and ongoing extension (Franke *et al.* 2015). Sinha *et al.* (2019) suggest that the basin is underlain by continental crust, based on interpretation of long-cable seismic reflection data. The basin is considered to be part of the southeastern offshore branch of the EARS, together with the Pemba, Mafia and Lacerda basins offshore Tanzania and Mozambique (Mougenot *et al.* 1986a; Chorowicz 2005). The EARS itself is a 5000 km long evolving divergent plate boundary enclosing three independently moving microplates (Saria *et al.* 2014). The extension rates decrease from higher rates in the north (5.2–6.5 mm yr^{-1}) to lower rates in the south (0.8–1.1 mm yr^{-1}; Stamps *et al.* 2008; Saria *et al.* 2014). The seismicity of the EARS mainly focuses onshore along its Eastern and Western Branches, with fewer and smaller earthquakes offshore. At present, its E–W extensional stress field is oriented perpendicular to the dominating N–S strike of major structures along the DFZ.

In contrast to the continental southern DR, several studies (Mougenot *et al.* 1986a; Franke *et al.* 2015) show that the seafloor topography north of 13°S off Mozambique is not related to any major basement structure but is instead a purely sedimentary feature. The northern segment's topography is thus not related to fracture zone tectonics.

The kinematic evolution of the North Mozambican to Somalian coasts during the Jurassic are not fully understood and thus numerous differing models exist. Seafloor spreading in the West Somali Basin ceased in Early Cretaceous times, leaving Madagascar as part of the African plate. The timing of the termination of seafloor spreading is controversial. One set of studies (Segoufin & Patriat 1980; Cochran 1988; Gaina *et al.* 2013; Davis *et al.* 2016; Phethean *et al.* 2016; Sauter *et al.* 2016) suggest that the spreading terminated early in chron M0r [soon after 125.9 Ma (Ogg 2012; magnetic timescale)]. Another set of studies (Rabinowitz *et al.* 1983; Coffin *et al.* 1986; Eagles & König 2008; Tuck-Martin *et al.* 2018) suggest a slightly older age (133.9–133.6 Ma; M10n). The lack of dense and systematic marine magnetic data and/or basement samples from the proposed location of the extinct spreading axis in the Somali Basin means that the problem of the timing of its extinction cannot currently be solved.

Few marine magnetic profiles are available to constrain the oldest seafloor spreading during the early evolution of the Somali Basin. This results in large uncertainties in the proposed extents and orientations of structures in the DFZ (Phethean *et al.* 2016; Sinha *et al.* 2019). Sinha *et al.* (2019) published the most extensive seismic study to date of the Tanzanian and North Mozambique margins, which is based on all available industry seismic reflection data. They propose that the margin segments offshore Tanzania and Kenya formed during oblique spreading leading to the development of pull-apart basins, whilst that off northern Mozambique developed as a pure strike-slip margin since 153 Ma. Using the same seismic data, however, interpretations of the position of the continent–ocean boundary (COB) off Kenya and Tanzania differ by up to 140 km (Sauter *et al.* 2018; Sinha *et al.* 2019). Offshore Tanzania, a prominent deep seismic reflector is interpreted as an asthenospheric diapir or lens of frozen melt beneath the oceanic crust of the West Somali Basin (Sauter *et al.* 2016; Sinha *et al.* 2019). Rabinowitz (1971) proposes that the DR is marked by a small relative gravity high (50 mGal) stretching across the West Somali Basin as far as the 300 mGal gravity high of the Walu Ridge near the Kenyan shore (Fig. 1). Coffin and Rabinowitz (1987) consider the DFZ to run along this high. Between 9°S and 20°S, Mahanjane (2012) continues to link the DFZ with a clear free air anomaly parallel to the coast. Taken together, these identifications imply the presence of a >1200 km long shear zone along the East African margin (Coffin & Rabinowitz 1987). However, none of the recent seismic reflection studies has been able to interpret a prominent DFZ in the basement north of 13°S (Klimke *et al.* 2018). Sinha *et al.* (2019) combine the DFZ with the adjacent Seagap Fracture Zone MacGregor 2018; Reeves 2018) to form the Davie Transform System (DTS), which connects the extensional margins of Somalia and Central Mozambique from the Walu Ridge through the Mozambique Channel to southern Madagascar. Part of the principal deformation zone of the DTS runs through the Kerimbas Basin. In contrast, Phethean *et al.* (2016) suggest the DFZ turns onshore near the Tanzanian coast

based on gravimetric interpretations (north of 13°S). Using satellite gravity data these authors mapped several small fracture zones in the northern Somali Basin. In summary, due to the absence of sufficient seismic refraction data there is no good structural control on the crustal variations within the DFZ.

3 DATA ACQUISITION AND PROCESSING

3.1 Seismic data

The wide-angle seismic lines AWI-20140130 and AWI-20140150 each consist of 20 sea-bottom stations equipped with ocean bottom seismometers (OBS) or ocean bottom hydrophones (OBH), which all recorded data on at least one component (Fig. 1b). The OBHs are equipped with a hydrophone, while the OBSs have an additional seismometer. The data are recorded at a sampling rate of 200 to 250 Hz (Jokat 2014). Eight G-Guns with 8.5 l volume each were towed in 4 × 2 clusters in 10 m water depth. Seismic pulses were released every minute at a pressure of 210 bars and with an average shot spacing of 150 m.

The length of each profile line is calculated between the first and last shot and the OBS/OBH positions are projected onto those lines. Instrument spacing along both profiles is about 9.5 km. No land stations could be deployed due to missing permits from the Mozambican government. Profile AWI-20140130 is situated at about 13°S and spans about 178 km in east–west direction. Line AWI-20140150 is located further to the north at 11.5°S and is 182 km long.

During processing, the recorded raw data are first converted into SEG-Y and corrected for the measured run-time error (skew) of the internal instrument clock. The drift of the instrument during the descent to the seafloor is adjusted for by relocalization using the direct water wave. The maximum shift is 118 m for instruments along AWI-20140130 and 560 m along AWI-20140150. The large offset is attributable to strong currents during the deployment/recovery. The data quality is good. In most cases, the hydrophone component shows the best data quality, but often the *z*-components of the seismometer data contains additional information on the phases (Tables 1 and 2) with long offsets.

3.2 Potential field data

For continuous gravity measurements the BGR-owned Bodenseewerke sea gravimeter system KSS32M (S/N 22) was used with a sampling rate of 1 Hz. During processing infrequent outliers are eliminated manually and a median filter of 300 s is applied to reduce noise. The free air gravity anomaly is calculated using the ship-based navigation data for the GRS80 normal gravity and Eötvös corrections (Jokat 2014). Reference measurements at the beginning and end of the cruise in Durban tie the data to the IGSN71 (Morelli *et al.* 1974). A small instrument drift of −0.02 mGal is observed over 50.778 days (Jokat 2014).

For acquiring magnetic data, a sensor array was towed approximately 750 m astern of the vessel. The array consisted of a SeaSpy gradient magnetometer array with two scalar Overhauser sensors and a Magson vector magnetometer sensor mounted between them, as well as two vector magnetometer sensors mounted on the observation deck above the bridge (Jokat 2014).

4 METHODS

4.1 Wide-angle seismic data modelling

The seismic data of both profiles are filtered with a bandpass filter of 3 to 17 Hz, and in order to enhance low-frequency phases, an automatic gain control (AGC) filter of 1 s was applied. Phase picking and identification are conducted using the *ZP*-software (Zelt 2004, http://www.soest.hawaii.edu/~bzelt/zp/zp.html). In a forward-modelling approach, layers are adjusted one-by-one to the picks, starting with the uppermost layer and working downwards to the mantle. *A priori* information including water depth and sediment layer geometries, was incorporated from seismic reflection data and swath bathymetry (Franke et al 2015; Klimke & Franke 2016). We used the graphical interface *PRay* (Fromm 2016, https://sourceforge.net/projects/pray-plot-rayinvr/), based on the *rayinvr* software (Zelt & Smith 1992, http://terra.rice.edu/department/faculty/zelt/rayinvr.html). A *P*-wave velocity model is created and refined with the inversion method based on damped least-squares (Zelt & Smith 1992). On profile AWI-20140150, only a few picks are made at more than 50 km offset. Data examples are shown for OBS 156 (Fig. 3) and OBS 163 of profile AWI-20140150 (Fig. 4) and OBS 139 (Fig. 5) of profile AWI-20140130 together with the phases identified and rays traced from them. All picks from all stations with the calculated travel time curves are presented in Figs 6 and 7.

4.2 Amplitude modelling

The *rayinvr* software uses a high-frequency approximation of the wave equation (Zelt & Smith 1992). This method traces rays at sharp edges or in highly variable topography (Jokat & Schmidt-Aursch 2007, Müller *et al.* 2016). Seismic velocities in deep crustal layers are only sparsely determined by refracted rays. To verify the topography and the velocities in the model, we utilize the finite difference (FD) program *SOFi2D* (Bohlen *et al.* 2016, https://git.scc.kit.edu/GPIAG-Software/SOFI2D) to calculate synthetic seismograms. Using this code, we calculate the propagation of waves in an inhomogeneous viscoelastic 2-D medium (Bohlen 1998). Tests have shown that the normalized amplitude variation of 2-D and 3-D modelling is comparable (Bohlen 1998; Bohlen, 2002). Thus, for 2-D *P*-wave velocity models a 2-D amplitude modelling provides acceptable results.

The signal amplitude of each phase provides a distinct amplitude pattern. The amplitude decreases with distance to the source, varies due to interference with other phases and contrasting velocities at layer boundaries. This pattern is obscured in the presence of either short phases (<20–30 km) or strong noise. The PmP-reflection can provide additional constraints on the velocity distribution of the lowermost layer. To utilize these constraints, we change the velocity at the crust–mantle boundary in 0.2 km s^{-1} steps and compare the normalized amplitude pattern of the observed and synthetic PmP-reflections. To achieve good fits, the Moho depth is varied without changes in the topography.

The model discretization in 25 m × 25 m cells leads to grid sizes of 7120 × 1400 cells for profile AWI-20140130 and 7280 × 1400 cells for AWI-2010150. The wave propagation is calculated for 30 s with a time step of 1 ms for numerical stability. The seismic source approximation is a Ricker wavelet of 5 Hz, placed at the instrument position. The seismic signal is recorded every 150 m, which is equivalent to the shot spacing. A strongly damping layer

Table 1. Statistics of picked phases and assignment of picked phases for profile AWI-20140150. The columns contain the labels of the picked phases and the respective layer, the number of picks and the number of traced picks, the root mean square of the traveltime residual and the normalized chi-squared value.

Phase	Picks	Traced picks	Percentage (per cent)	Uncertainty t_{picks}	t_{RMS}	χ^2
12	2148	2127	99.0	0.084	0.047	0.358
22	411	407	99.0	0.150	0.081	0.291
31	556	472	84.9	0.082	0.043	0.429
32	559	549	98.2	0.149	0.068	0.213
41	493	461	93.5	0.085	0.049	0.466
42	663	586	88.4	0.140	0.115	0.706
51	558	504	90.3	0.095	0.068	0.704
52	1034	945	91.4	0.136	0.098	0.604
61	1094	1033	94.4	0.091	0.073	0.827
62	694	650	93.7	0.140	0.093	0.487
71	938	919	98.0	0.113	0.107	1.284
72	776	698	89.9	0.133	0.118	0.937
81	941	875	93.0	0.128	0.140	1.343
82	740	740	100.0	0.138	0.121	0.850
91	84	80	95.2	0.138	0.212	3.333
92	263	263	100.0	0.141	0.157	1.291
101	419	418	99.8	0.136	0.156	1.503
ALL	12378	11734	94.8	0.116	0.097	0.749

Table 2. Statistics of picked phases and assignment of picked phases for profile AWI-20140130. The columns contain the labels of the picked phases and the respective layer, the number of picks and the number of traced picks, the root mean square of the traveltime residual and the normalized chi-squared value.

Phase	Picks	Traced picks	Percentage (per cent)	Uncertainty t_{picks}	t_{RMS}	χ^2
12	4080	4038	99.0	0.082	0.033	0.302
21	77	54	70.1	0.091	0.093	1.507
22	402	393	97.8	0.180	0.087	0.236
31	841	764	90.8	0.077	0.042	0.521
32	1276	1105	86.6	0.170	0.074	0.271
41	918	829	90.3	0.118	0.073	0.577
42	1387	1352	97.5	0.167	0.088	0.372
51	539	511	94.8	0.071	0.061	0.878
52	755	736	97.5	0.172	0.099	0.374
61	1595	1544	96.8	0.080	0.050	0.539
62	1574	1530	97.2	0.151	0.107	0.567
71	1183	1112	94.0	0.104	0.074	0.811
72	724	662	91.4	0.162	0.113	0.485
81	1960	1945	99.2	0.111	0.105	1.199
82	1757	1679	95.6	0.161	0.154	1.149
92	460	422	91.7	0.166	0.344	4.932
101	1810	1619	89.4	0.153	0.291	4.456
ALL	21388	20295	94.9	0.125	0.126	0.998

is incorporated (10 grid cells, 250 m) on the lateral and lower boundaries, while the upper boundary is a free surface.

The input parameters for the program are the *P* and *S*- wave velocity fields, the density distributions and the attenuations for *P* and *S*- waves. The *P*-wave velocities were converted into *S*-wave velocities with the simple $\sqrt{3}$ conversion. The density values are calculated from the velocity–density relationship of Nafe & Drake (1957). The seismic attenuation of the layers is calculated according to Brocher (2008) from the *P*-wave velocity model of both profiles, with the attenuation of water added manually.

Similar to the observed data, a bandpass filter of 3–17 Hz and an AGC filter of 1 s are used. The PmP phase is picked with *ZP* (Zelt 1999) and the amplitude values are retrieved. A median envelope of 3 km best compensates the noise in the observed data. The same filter is applied to the synthetic data. Amplitude modelling results are shown for OBS 159 (Fig. 8), which shows a PmP-reflection with sufficient quality to verify the eastern lower crustal velocity of profile AWI-20140150. OBS 143 (Fig. 9) and OBS 136 (Fig. 10) verify the velocity structure of the southern profile.

4.3 Error analysis of the *P*-wave velocity model

Information on the certainty of the model is provided by two values for *rayinvr*, the t_{RMS} misfit (root mean square) and χ^2-values (Zelt & Smith 1992). The optimal χ^2-value is 1, whereas smaller χ^2-values indicate a detailed model that is not uniquely determined by the picks, and greater values indicate that not all picks are fitted. The t_{RMS} misfit should be close to zero because it expresses the difference between the calculated travel time path and the observed pick. Pick uncertainties of between 55 and 200 ms are used relative

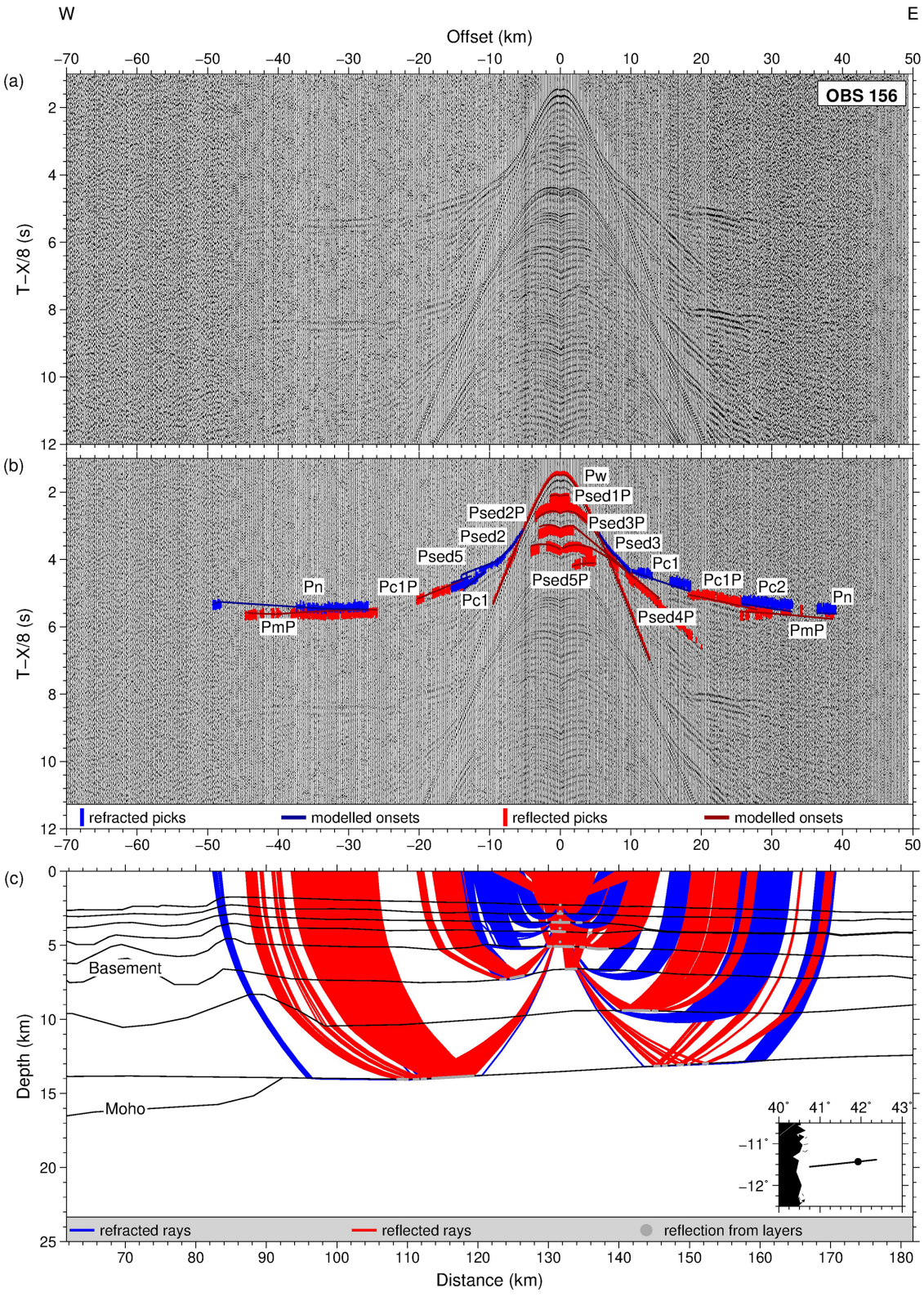

Figure 3. Data example of OBS 156 (Hydrophone) of profile AWI-20140150. (a) Hydrophone component filtered with a bandpass filter of 3–17 Hz. A reduction velocity of 8 km s^{-1} is applied for displaying the data. (b) Observed seismograms as in a), overlain with picked phases shown as error bars according to the signal to noise ratio. Refracted arrivals are plotted in red, reflected in blue. The arrivals modelled with RAYINVR are shown as red and blue lines. (c) Modelled ray paths of the picks shown in b) and the sampled part of the model. The direct water wave is labelled Pw and refracted phases in the sediments Psed1, Psed2, etc., while reflections from the sedimentary layers are labelled Psed1P, Psed2P, etc. The refracted crustal phases are named Pc1 and Pc2, the reflections are called Pc1P and Pc2P. Refracted and reflected phases from the high velocity lower crustal body (HVLCB) are called PcHVLCB and PCHVLCBP. Pn is the refracted phase from the upper mantle, PmP the reflection from the Mohorovičić discontinuity.

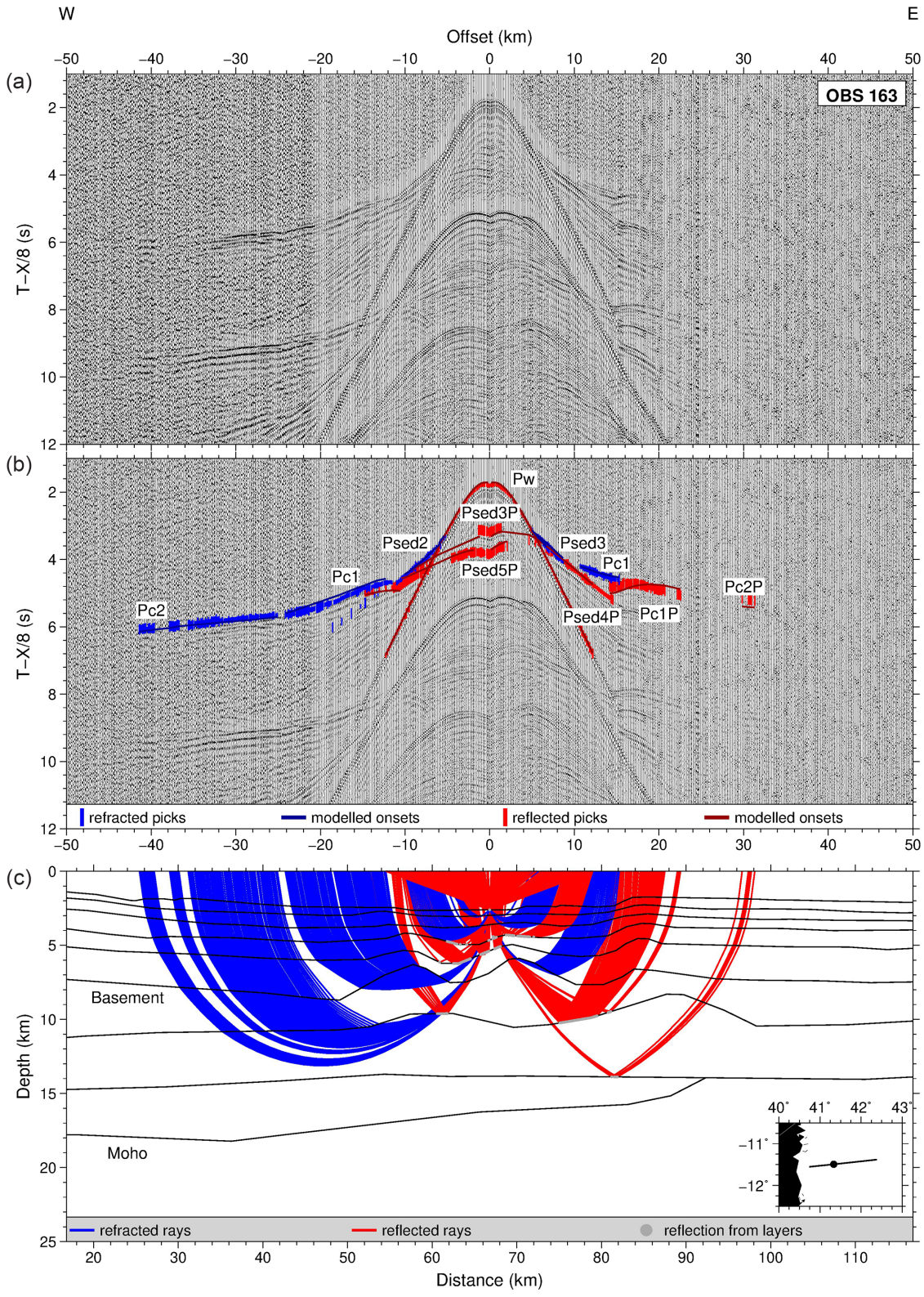

Figure 4. Data example of OBS 163 (Hydrophone) of profile AWI-20140150. (a) Hydrophone component filtered with a band-pass filter of 3–17 Hz. A reduction velocity of 8 km s^{-1} is applied for displaying to the data. (b) Observed seismograms as in (a), overlain with picked phases shown as error bars according to the signal to noise ratio. Refracted arrivals are plotted in red, reflected in blue. The arrivals modelled with RAYINVR are shown as red and blue lines. (c) Modelled ray paths of the picks shown in b) and the sampled part of the model. See the description of Fig. 3 for labelling.

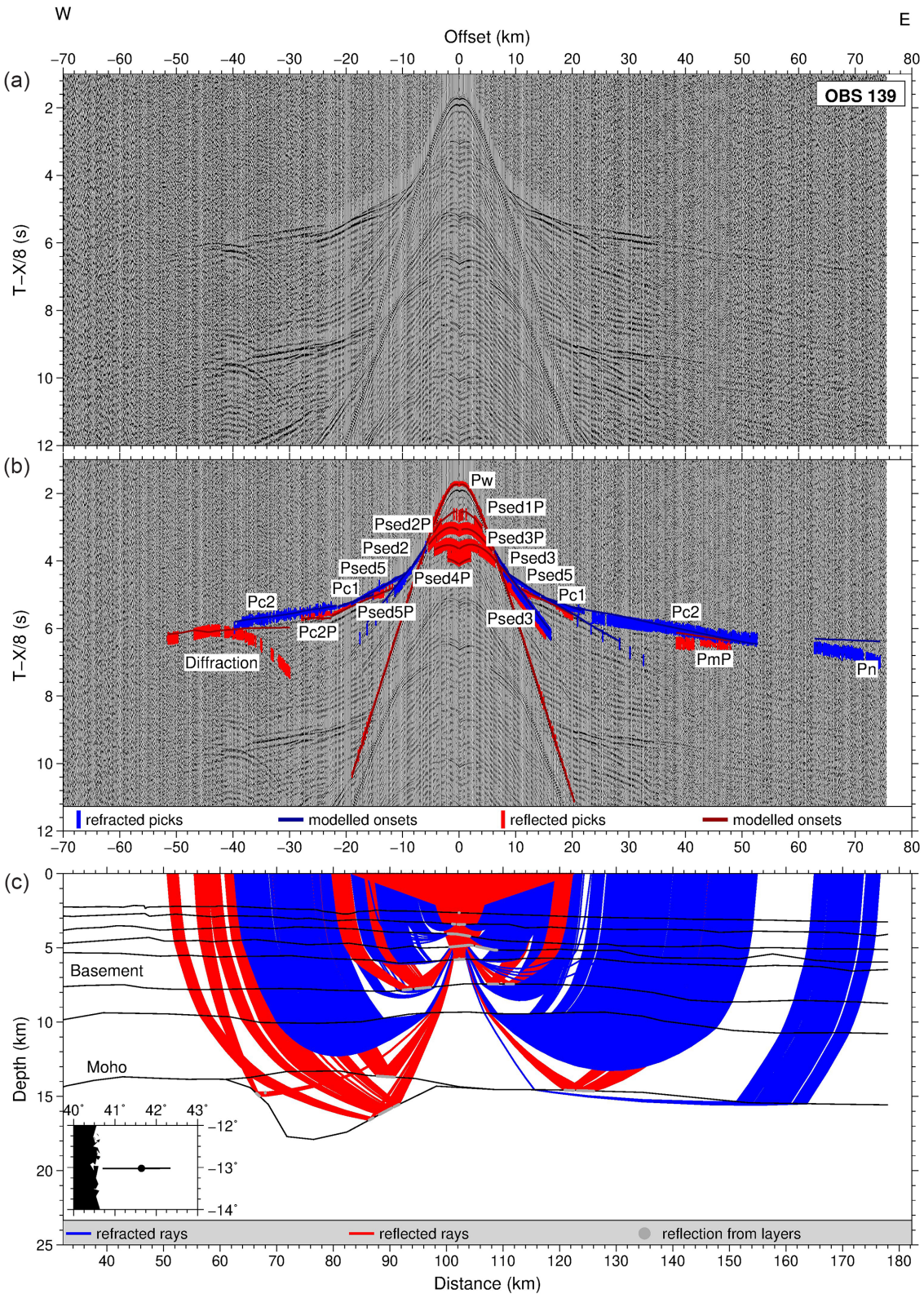

Figure 5. Data example of OBS 139 (Hydrophone) of profile AWI-20140130. (a) Hydrophone component filtered with a band-pass filter of 3–17 Hz. A reduction velocity of 8 km s^{-1} is applied for displaying to the data. (b) Observed seismograms as in (a), overlain with picked phases shown as error bars according to the signal to noise ratio. Refracted arrivals are plotted in red, reflected in blue. The arrivals modelled with RAYINVR are shown as red and blue lines. (c) Modelled ray paths of the picks shown in b) and the sampled part of the model. See the description of Fig. 3 for labelling.

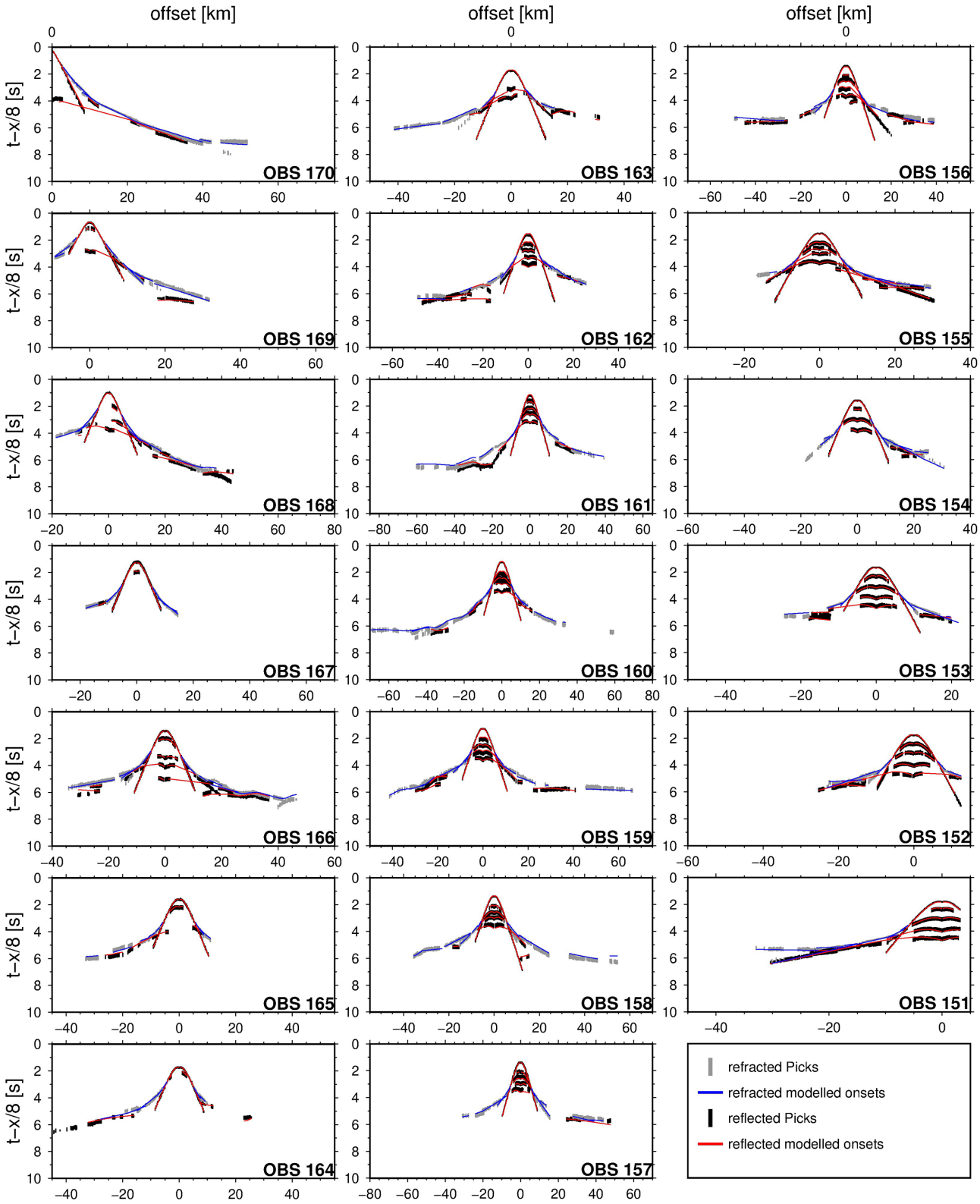

Figure 6. All stations of line AWI-20140150 with the picked uncertainties are shown as black (reflected) and grey (refracted) error bars. Modelled arrivals are marked in blue and red.

to the signal-to-noise ratio, leading to a mean uncertainty of 0.125 s for profile AWI-2040130 and 0.116 s for profile AWI-20140150.

For the southern profile (AWI-20140130), we picked 21 388 onsets, of which nearly 95 % can be traced. An RMS misfit for all phases of 0.126 s is close to the mean uncertainty of 0.125 s. The χ^2-value is 0.998. On the northern profile, nearly 95 % of 12 378 onsets can be traced. Here, a smaller χ^2-value of 0.749 is calculated and the t_{RMS} misfit of 0.097 s is smaller than the mean pick

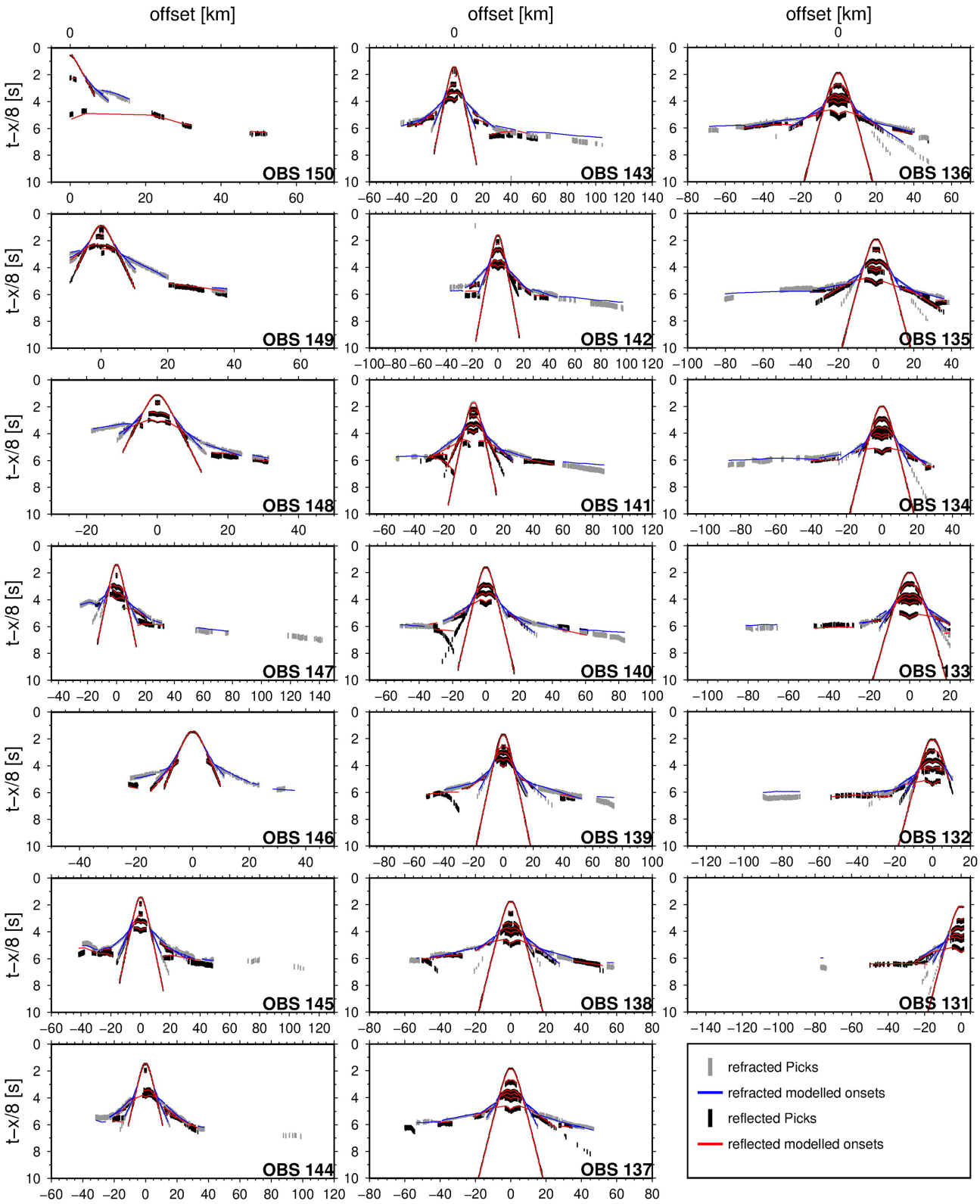

Figure 7. All stations of line AWI-20140130 with the picked uncertainties are shown as black (reflected) and grey (refracted) error bars. Modelled arrivals are marked in blue and red.

uncertainty of 0.116 s. The achieved values, uncertainties and t_{RMS} errors for each layer are listed in Tables 1 and 2 for both profiles.

To determine the uncertainties of each layer, Schlindwein and Jokat (1999) change single depth points or velocity nodes, without altering the fit of the model. We follow this scheme for some representative points and nodes of each model. This method leads to uncertainties at the layer boundaries of 0.5 km for the sediments, 1 km for the upper crust and 2 km for the lower crust and the mantle.

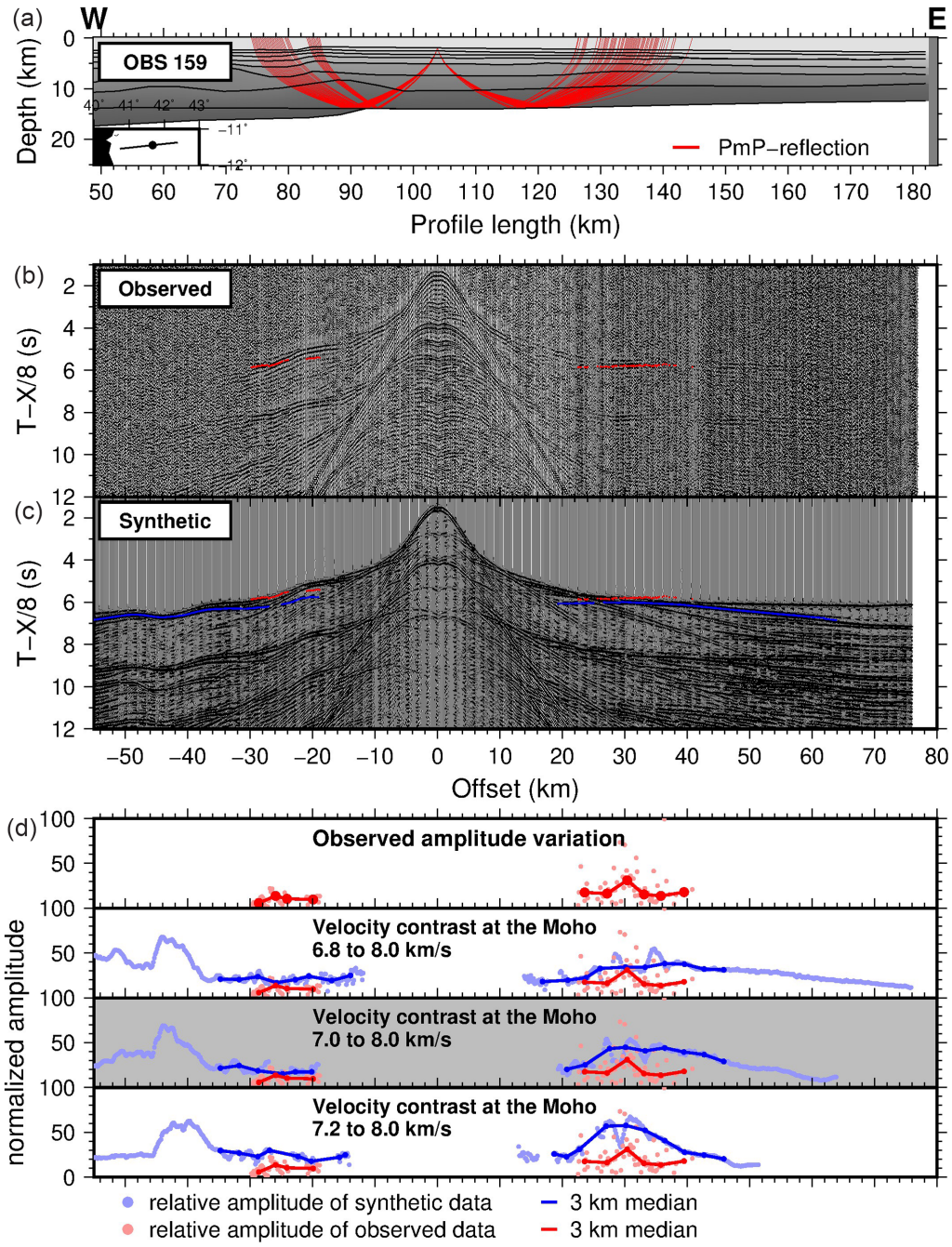

Figure 8. Synthetic amplitudes modelled with SoFi2D (Bohlen *et al.* 2016) for OBS 159 of profile AWI-20140150. (a) The ray path of the PmP-Reflection from HVLCB- Mantle boundary. (b) Observed seismogram with picks for the PmP-reflection (c) Synthetic seismogram for the final model with picks of the synthetic PmP- reflection. Both seismograms are filtered with 3–17 Hz and an AGC filter of 1 s is applied. (d) Amplitude patterns for four different velocity contrasts for the model. The best model is underlain in grey.

Velocity uncertainties range from 0.1 km s^{-1} in the sediments to 0.2 km s^{-1} for the crust and mantle. This fits to an observed change of the amplitude pattern by varying the lower crustal velocities of 0.2 km s^{-1}. The achieved uncertainties and layer parameters for each layer are presented in Tables 3 and 4 for the southern and northern profiles, respectively.

The ray coverage of the models influences the resolutions of modelled velocities. Zelt & Smith (1992) describe an inversion method to calculate the resolution. The resolution is perfect for a value of 1 and not at all constrained by rays at a value of 0. Values between 0.5 and 1 are normally considered as well-resolved (Zelt 1999; Altenbernd *et al.* 2014; Müller *et al.* 2016). Direct velocity information is available in areas covered by refracted rays (Figs 11 and 12; left columns), whereas reflected rays provide implicit velocities (Figs 11 and 12; right columns).

The ray coverage of Profile AWI-20140150 is good for the sedimentary layers (Fig. 11). The eastern part of the oceanic layer 2 and the upper half of oceanic layer 3 are well covered with refracted rays. Reflections image the Moho on the eastern side. The upper and middle crust of the western side is well covered,

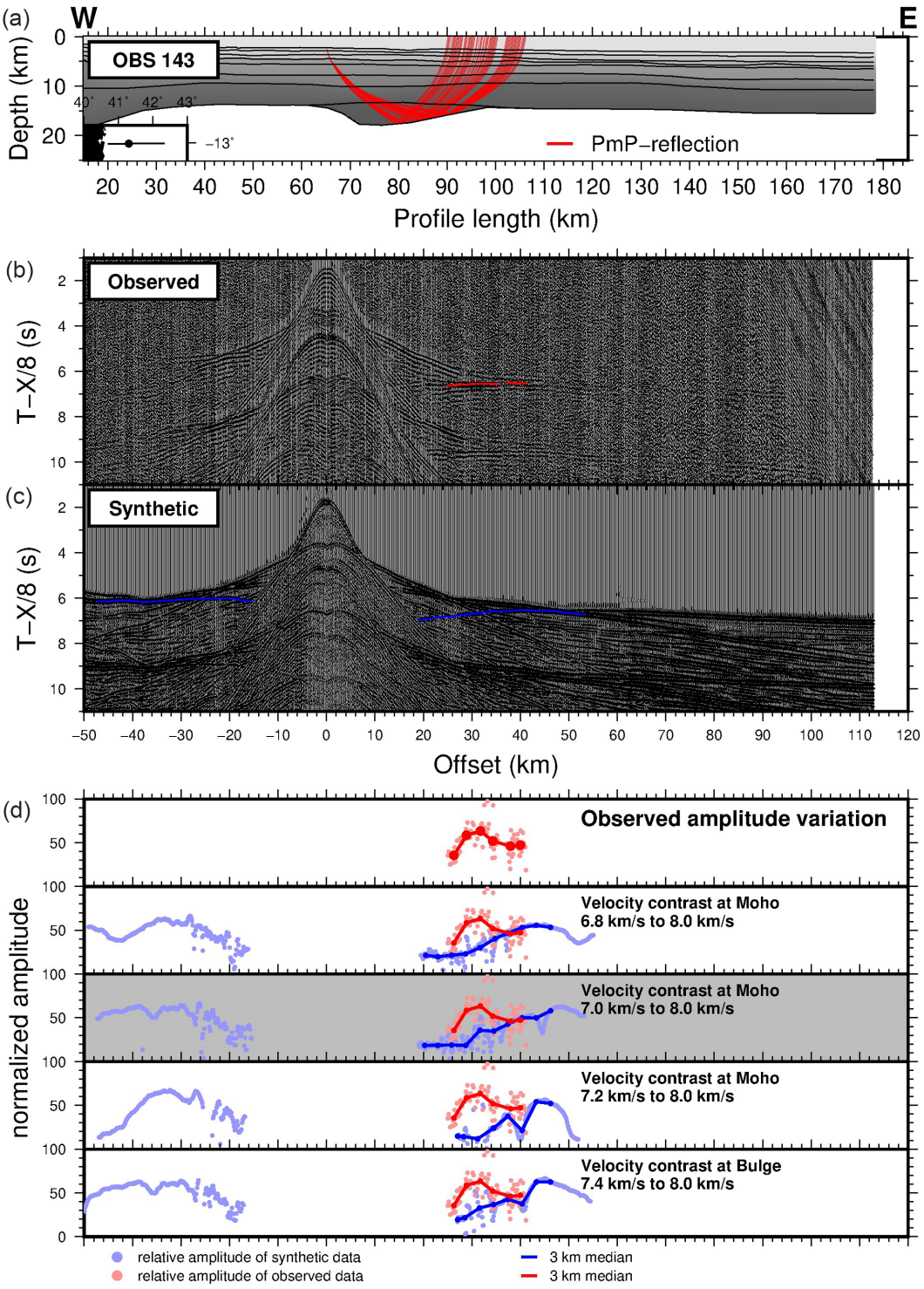

Figure 9. Synthetic amplitudes modelled with SoFi2D (Bohlen *et al.* 2016) for OBS 143 of profile AWI-20140130. (a) The ray path of the PmP-Reflection from HVLCB–Mantle boundary. (b) Observed seismogram with picks for the PmP-reflection. (c) Synthetic seismogram for the final model with picks of the synthetic PmP-reflection. Both seismograms are filtered with 3–17 Hz and an AGC filter of 1 s is applied. (d) Amplitude patterns for four different velocity contrasts for the model. The best model is underlain in grey.

but the lowermost layer has only sparse ray coverage in both reflected and refracted rays (Fig. 11). Almost no rays are observed in the mantle. Large parts of the sediments have a resolution greater than 0.5, except for the topographic Kerimbas Basin (Fig. 13a). The crustal layer resolutions are near 0.5 and thus less well resolved.

Profile AWI-20140130 has a good coverage of reflected and refracted rays in the sedimentary units (Fig. 12). The resolution in the sediments is in large parts near 1, and thus well resolved (Fig. 13b). The underplated material (HVLCB: High Velocity Lower Crustal Body) has a resolution of less than 0.5, since only reflected phases are observed, but velocities are calculated with amplitude modelling

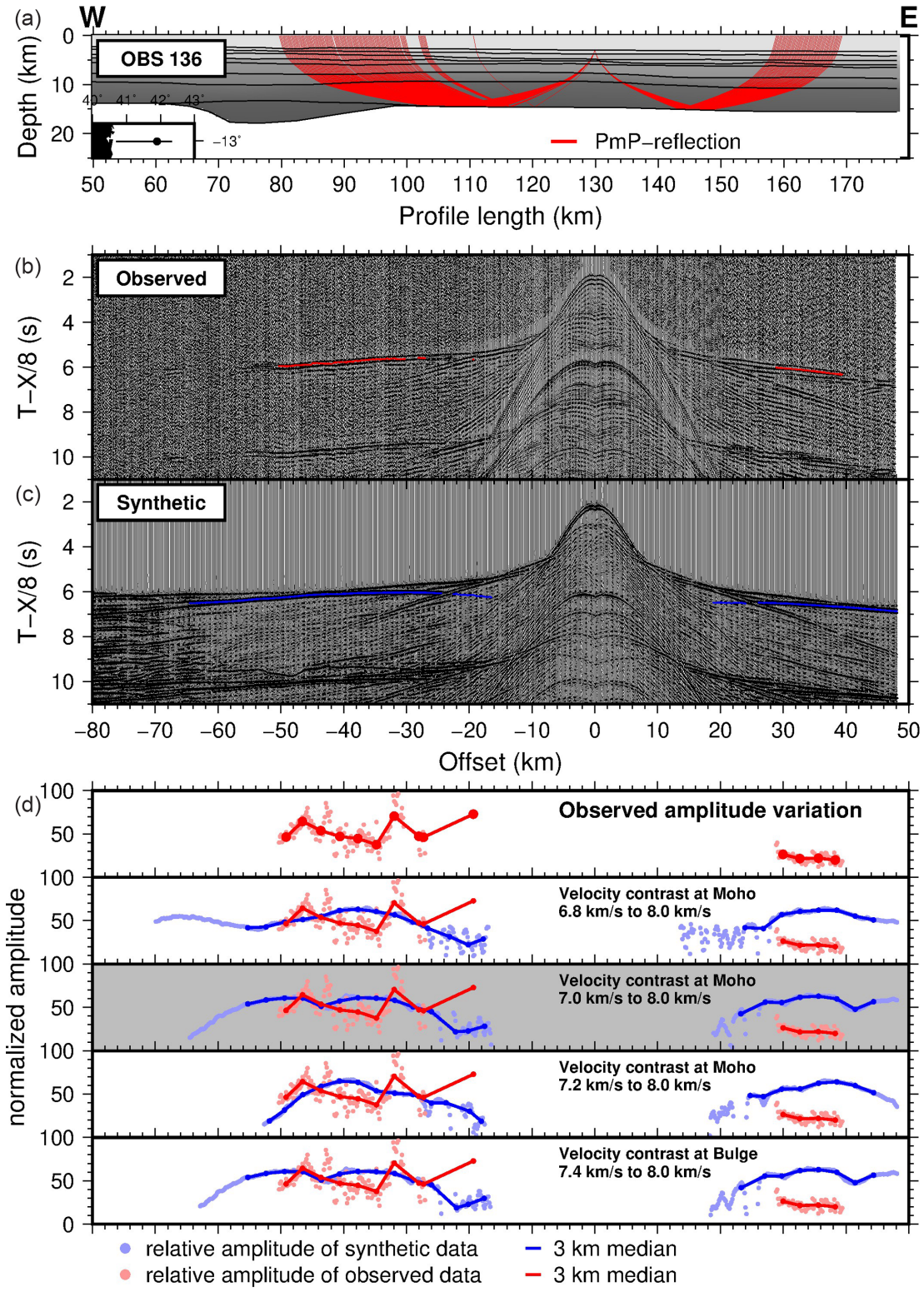

Figure 10. Synthetic amplitudes modelled with SoFi2D (Bohlen *et al.* 2016) for OBS 136 of profile AWI-20140130. (a) The ray path of the PmP-Reflection from HVLCB–Mantle boundary. (b) Observed seismogram with picks for the PmP-reflection. (c) Synthetic seismogram for the final model with picks of the synthetic PmP-reflection. Both seismograms are filtered with 3–17 Hz and an AGC filter of 1 s is applied. (d) Amplitude patterns for four different velocity contrasts for the model. The best model is underlain in grey.

(Fig. 9). The velocity uncertainty for the modelled HVLCB lies approximately by 0.2 km s^{-1}, its thickness uncertainty is up to 2 km, and the uncertainty in its horizontal position is 10 km. The eastern part of the crust is well covered by refracted and reflected rays, its resolution exceeds 0.5, and is additionally constrained by amplitude modelling (Fig. 10).

Table 3. Layer parameters of profile AWI-20140150 and according uncertainties. *P*-wave velocities and densities vary in one respective layer due to differences in geology.

Layer	Type	Max. thickness [km (profile km)]	*P*-wave velocity (km s^{-1})	Density range (g cm^{-3})	Upper boundary uncertainty (km)	Velocity uncertainty (km s^{-1})
Water	Water	2.79 (176)	1.5	1.03	±0.0	±0.1
Sediment	Sedimentary layer 1	0.8 (32)	1.8–2.1	1.98	±0.5	±0.1
	Sedimentary layer 2	1.0 (159)	2.0–2.6	2.09	±0.5	±0.1
	Sedimentary layer 3	1.4 (23)	2.6–3.2	2.35	±0.5	±0.1
	Sedimentary layer 4	1.6 (61)	3.0–3.9	2.42	±0.5	±0.1
	Sedimentary layer 5	2.7 (49)	4.3–4.8	2.49	±0.5	±0.1
Upper crust	Upper crust Kerimbas Basin	4.7 (70)	5.0–5.7	2.63	±1.0	±0.2
	Oceanic layer 2	3.2 (102)	5.3–6.2	2.66	±1.0	±0.2
Middle crust	Middle crust Kerimbas Basin	5.7 (89)	5.8–6.8	2.75	±1.0	±0.2
	Oceanic layer 3	4.1 (134)	6.4–7.1	2.88	±1.0	±0.2
Lower crust	Lower crust Kerimbas Basin	3.9 (35)	6.7–7.1	2.95	±3.0	±0.3
Mantle	Mantle		7.9	3.24	±3.0	±0.3
	Mantle		8.0	3.28	±2.0	±0.2

Table 4. Layer parameters of profile AWI-20140130 and according uncertainties. *P*-wave velocities and densities vary in one respective layer due to differences in geology.

Layer	Type	Max. thickness [km (profile km)]	*P*-wave velocity (km s^{-1})	Density range (g cm^{-3})	Upper boundary uncertainty (km)	Velocity uncertainty (km s^{-1})
Water	Water	3.25	1.5	1.03	±0.0	±0.1
Sediment	Sedimentary layer 1	0.9 (176)	1.8–2.0	1.86	±0.5	±0.1
	Sedimentary layer 2	1.2 (140)	2.2–2.7	2.09	±0.5	±0.1
	Sedimentary layer 3	1.2 (76)	2.5–3.4	2.18	±0.5	±0.1
	Sedimentary layer 4	1.8 (24)	3.1–4.5	2.39	±0.5	±0.1
	Sedimentary layer 5	2.5 (147)	4.5–4.9	2.50	±0.5	±0.1
Upper crust	Transitional crust (km 30–60)	2.3 (31)	5.2–5.7	2.68	±1.0	±0.2
	Oceanic layer 2 (km 60–110)	2.4 (73)	5.2–5.9	2.70	±1.0	±0.2
	Oceanic layer 2 (km 110–178)	2.2 (163)	5.1–6.1	2.70	±1.0	±0.2
Lower crust	Transitional crust (km 30–60)	4.6 (32)	6.3–6.9	2.70–2.80	±2.0	±0.2
	Oceanic layer 3 (km 60–110)	5.1 (61)	6.0–6.9	2.80	±2.0	±0.2
	Oceanic layer 3 (km 110–178)	5.3 (135)	6.5–7.1	2.92	±2.0	±0.2
HVLCB	High velocity lower crustal body (km 50–110)	3.80 (74)	7.0–7.2	2.91	±2.0	±0.2
Mantle	Mantle (km 30–60)		8.0	3.33	±2.0	±0.2
	Mantle (km 60–110)		7.8	3.27	±2.0	±0.2
	Mantle (km 110–178)		8.0	3.30	±2.0	±0.2

4.4 Gravity modelling

A 2.5D density model is calculated with the interactive program *IGMAS+* (Götze & Lahmeyer 1988; Götze 2007; Schmidt *et al.* 2007) to test the velocity structure. The density model is extended 100 km to both sides and additionally stretched orthogonal to the profile line to reduce edge effects. The parallel sections are connected with their neighbours via triangulation and the gravity response of the resulting bodies is calculated. For the starting geometry, the *P*-wave velocity model is transferred into a density model using a velocity–density conversion (Nafe & Drake 1957). The layer depth is kept fixed in all ray-covered areas. The densities are compared to Gardner *et al.* (1974), Leinweber *et al.* (2013), and Vormann *et al.* (2020) and adjusted to fit the observed ship-based gravity. Velocity changes throughout the profiles are addressed by dividing the layers into blocks and assigning different densities. The gravity grid of Sandwell *et al.* (2014) is used where no shipboard data are available. The aim is for the residual gravitational accelerations in the two models to be smaller than ±10 mGal (Ljones *et al.* 2004).

5 RESULTS

The final *P*-wave velocity and density models are presented together with the measured and calculated gravity and our interpretations of the results (Figs 14 and 15). The geometries of the sedimentary basins and basement topography are constrained by either coincident (AWI-20140130) or nearby parallel (2 km northwards, AWI-20140150) seismic reflection lines (Fig. 16; Franke *et al.* 2015; Klimke & Franke 2016).

Gravity and marine magnetic data acquired along the profiles complement the geophysical data set (Jokat 2014) to map structural differences. While the northern basin is associated with a gravity low

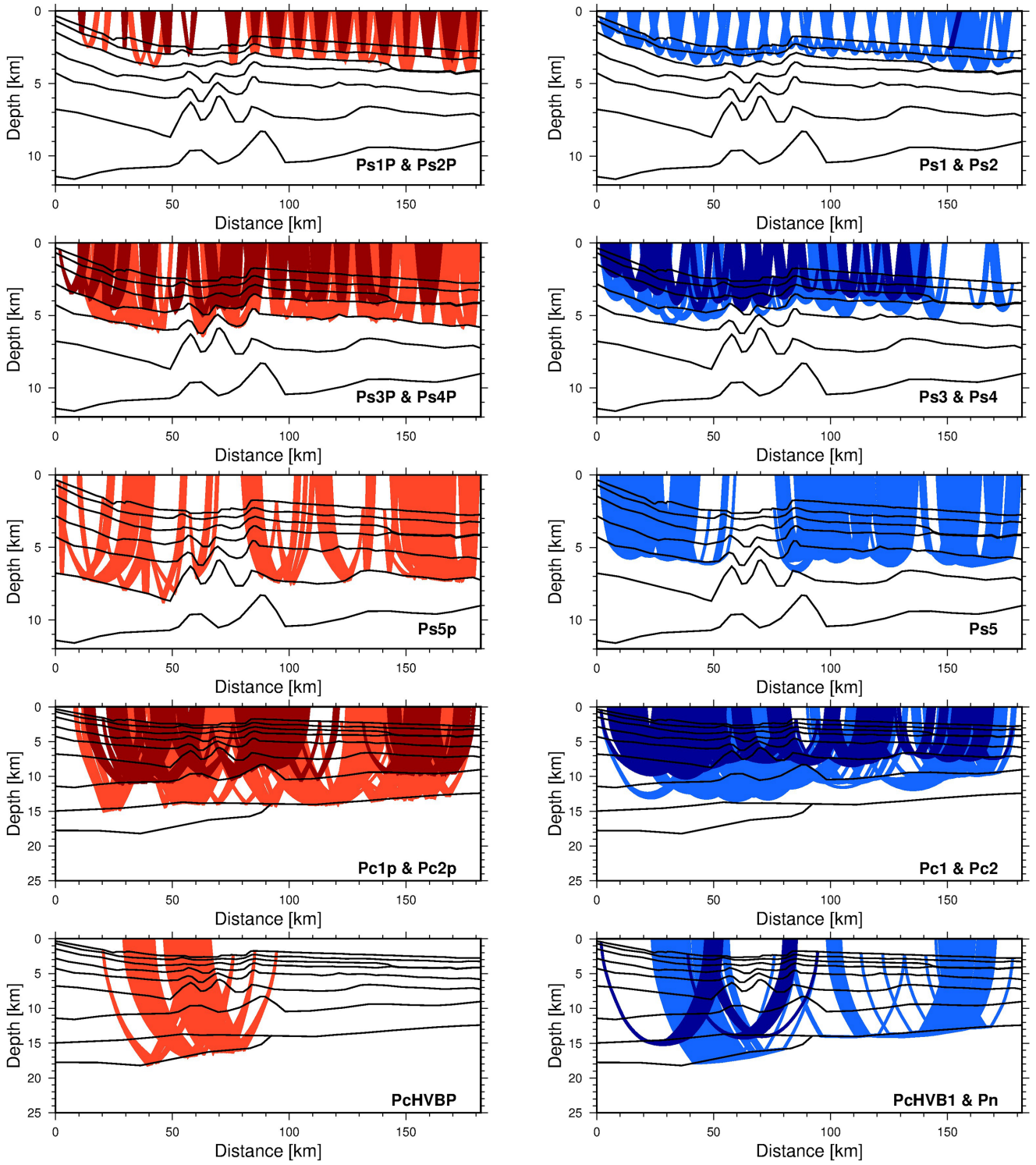

Figure 11. Ray coverage of the *P*-wave velocity model of reflected (red) and refracted (blue) waves for each layer for profile AWI-20140150.

of more than 120 mGal (AWI-20140150), its amplitude decreases southwards to ∼60 mGal were our line AWI-20140130 crosses the basin (Fig. 1b). At 11°S to 12°S, the orientation of the basin axis changes to NNE, and the seaward basin margin becomes subdued. St. Lazare Seamount lies between the two seismic profiles, where it is marked by an isolated positive gravity anomaly (Fig. 1b). Finally, no magnetic spreading anomalies could be identified within the Kerimbas Basin.

5.1 Line AWI-20140150 (Kerimbas Basin)

For brevity, and to avoid misunderstanding with distances in general, we refer in the following to distances along the profiles, for example, as ‘km 30’, which should be taken to mean the same as ‘30 km from the start of the profile’.

The northern profile crosses the central part of the Kerimbas Basin between 41.2°E and 41.5°E at 11.5°S. The velocity model

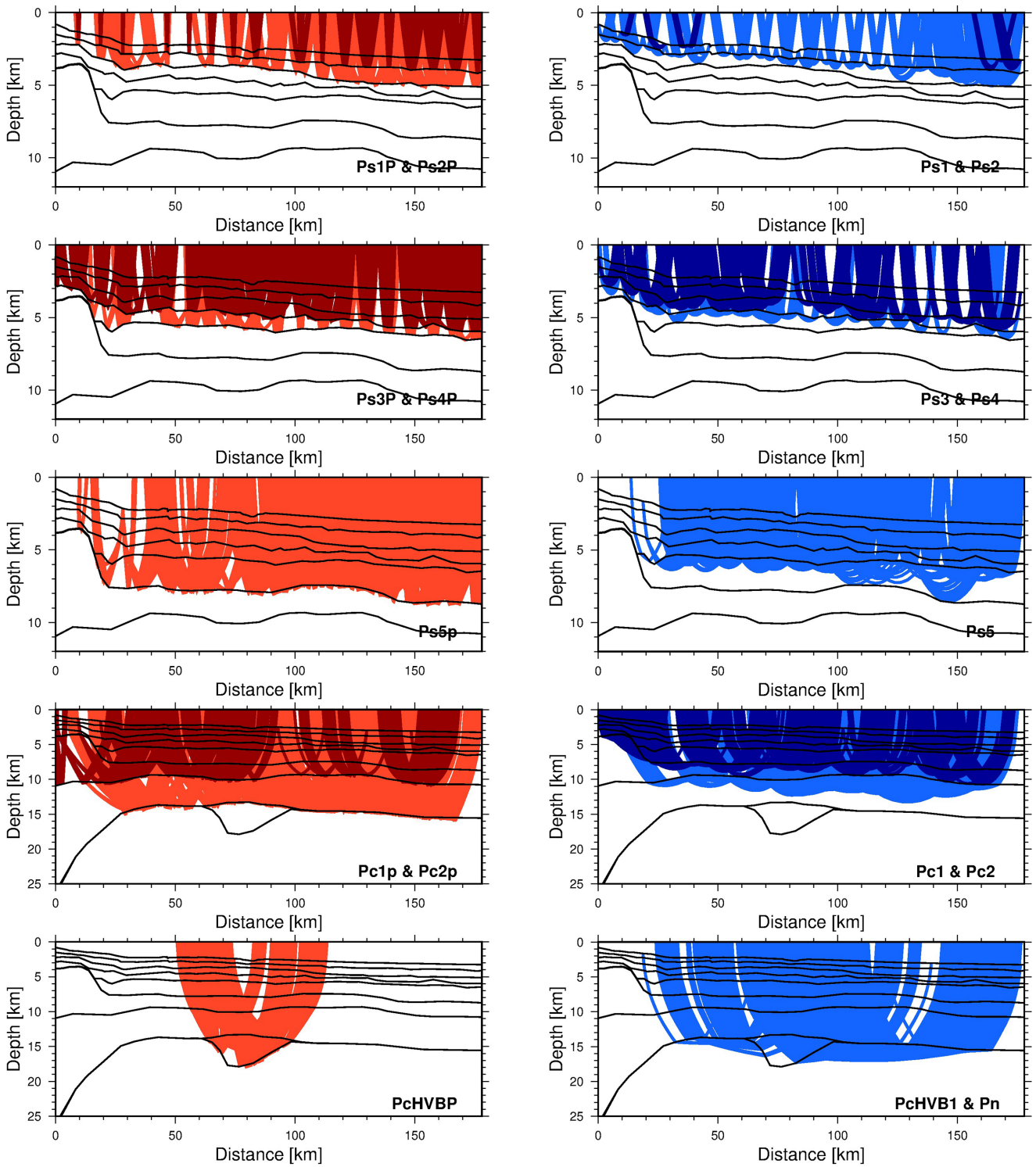

Figure 12. Ray coverage of the *P*-wave velocity model of reflected (red) and refracted (blue) waves for each layer for profile AWI-20140130.

(Fig. 14) consists of one water and one mantle layer, and eight intervening velocity layers: five sedimentary with differing gradients, and three crustal. The water depth deepens from 860 m at the western end of the profile near the Mozambican coast to 2730 m at km 82 in the Kerimbas Basin (Fig. 14). Beyond this, the eastern shoulder of the Kerimbas Basin, associated with the DR (km 100), shallows to 2190 m, after which the seafloor deepens again to 3250 m by the eastern end of the profile in the Comoros Basin.

Velocities in the uppermost sediment layer range from 1.7 km s^{-1} in the Kerimbas Basin (km 60–100) to 1.9 km s^{-1} in the Comoros Basin. Vertically, the velocities increase up to 4.4–4.8 km s^{-1} at the top of basement (Figs 14 and 16a; Table 3). No abrupt velocity jumps of more than 0.5 km s^{-1} are observed between sedimentary layers. The average total sediment thickness is 4–5.5 km with a maximum of 6.3 km (km 60–100). Both, the multichannel seismic data (Fig. 16a) and the seismic refraction data (Fig. 6; OBS 160–162)

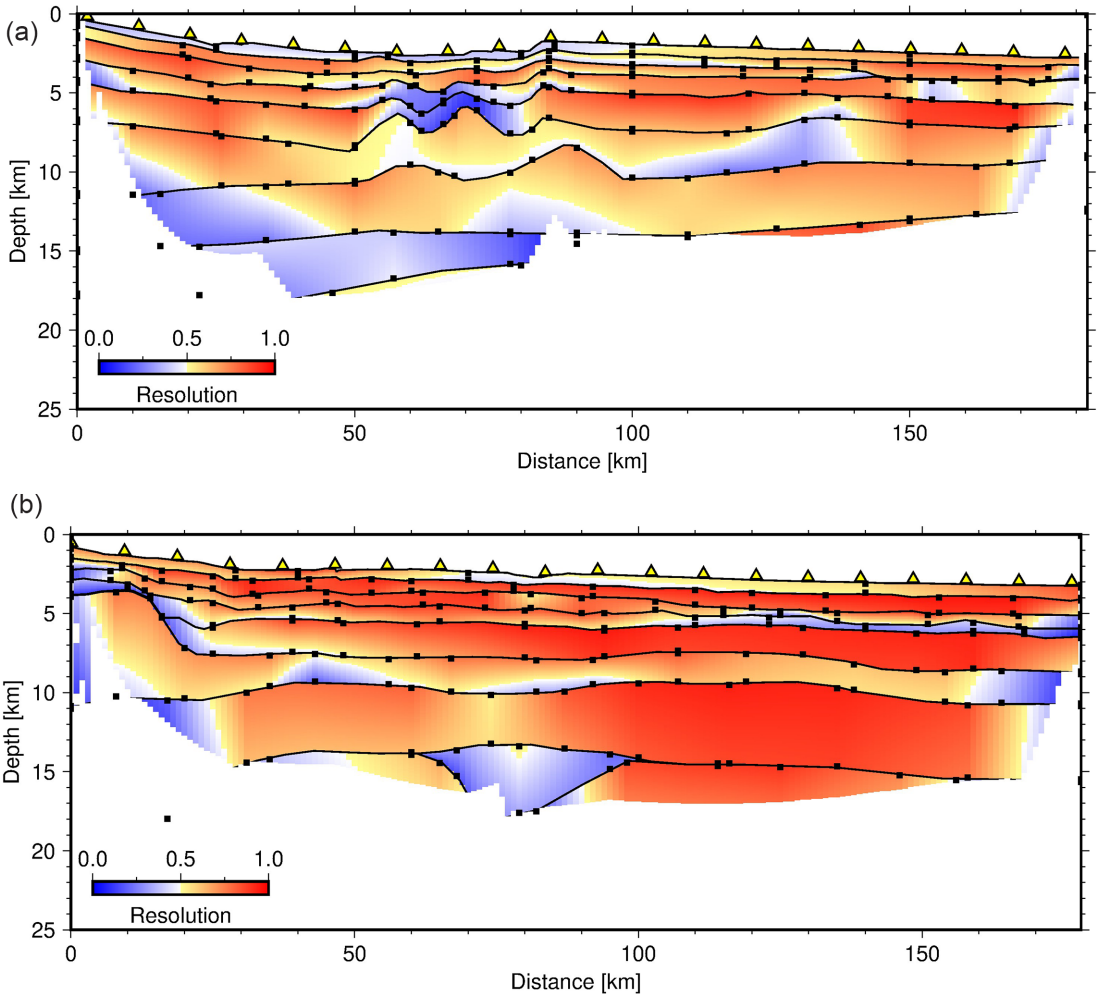

Figure 13. Resolution of the *P*-wave model of profile (a) AWI-20140150 and (b) AWI-20140130, represented by the diagonal elements of the resolution matrix. The value one indicates a perfect resolution, while zero means no resolution at all. Black dots mark the position of the velocity nodes that were used for the calculation. Yellow triangles indicate OBS/OBH positions.

imaged the basement topography in the Kerimbas Basin showing to be considerably smoother in the east (km 110–182). The assigned sediment densities for the subsequent gravity modelling range from 1.98 to 2.53 g cm^{-3} (Fig. 14; Table 3).

In the west (km 0–105) the crust consists of three velocity layers. The uppermost layer starts with a velocity of 5.0/5.2 km s^{-1} increasing up to 5.5 km s^{-1}. The thickness of the upper crust varies between 1.8 and 3.8 km. Its mean thickness is 2.5 km. The second crustal layer has velocities increasing with depth from 5.6 to 6.7 km s^{-1}. The thickness is up to 4 km. The third crustal layer shows velocities between 6.8 and 7.0 km s^{-1} and a thickness of 3 km. It is sparsely covered by rays (Fig. 11; km 30–90, depth range of 12–15 km), and therefore we have no strong constraints on its velocity (Fig. 13a). The PmP reflections recorded at two stations (OBS 159 and OBS 160; Figs 6 and 8) show no clear amplitude variations to further constrain velocities with amplitude modelling. The overall thickness of the crust beneath the Kerimbas Basin varies between 5.6 km and 8 km. The assigned densities for the upper crust vary between 2.7 g cm^{-3} in the first 60 km of the profile and 2.66 g cm^{-3} from km 60–110, and between 2.80 and 2.92 g cm^{-3} in the second layer. Densities in the third, lower-crustal, layer range from 2.95 to 2.98 g cm^{-3}. Although seismically less well-constrained, this third layer is necessary for the gravity model to reproduce the strong gravity minimum across the Kerimbas Basin without more significant changes to the seismic velocity model. The landward deepening of the Moho west of km 50 is only constrained by gravity modelling and westwards extrapolation of the modelled seismic layers. A maximum gravity-modelled crustal thickness of 15 km is reached at the western end of the profile. Extrapolating the crustal layers to the region beneath Mozambique, a crustal thickness of 30 km would be reached a further 80 km west of the western end of the profile.

In the eastern part of the profile over the Comoros Basin (km 110 onwards), the first crustal layer has a velocity of 5.4 km s^{-1} that increases up to 6.0 km s^{-1}. Its thickness smoothly varies between 1.5 and 2.5 km, with a steep velocity gradient of 0.17 to 0.37 s^{-1}. The assigned density is 2.66 g cm^{-3}. The underlying layer has a thickness of between 2.1 and 4 km, and its velocities range from 6.5 to 7.1 km s^{-1}. The modelled density is 2.92 g cm^{-3}. Only very few stations recorded arrivals with offsets of more than 50 km (OBS 160, 159, 158, 156, Fig. 6). For example, OBS 159 recorded signals up to km 60, with a high signal-to-noise ratio that allows us to observe an amplitude variation with a small maximum at km 34, and to compare it to synthetic seismograms (Fig. 8). In total, five OBS/OBH stations (169, 162, 161, 160, 159) in the middle and eastern parts of the line recorded refracted arrivals from the mantle

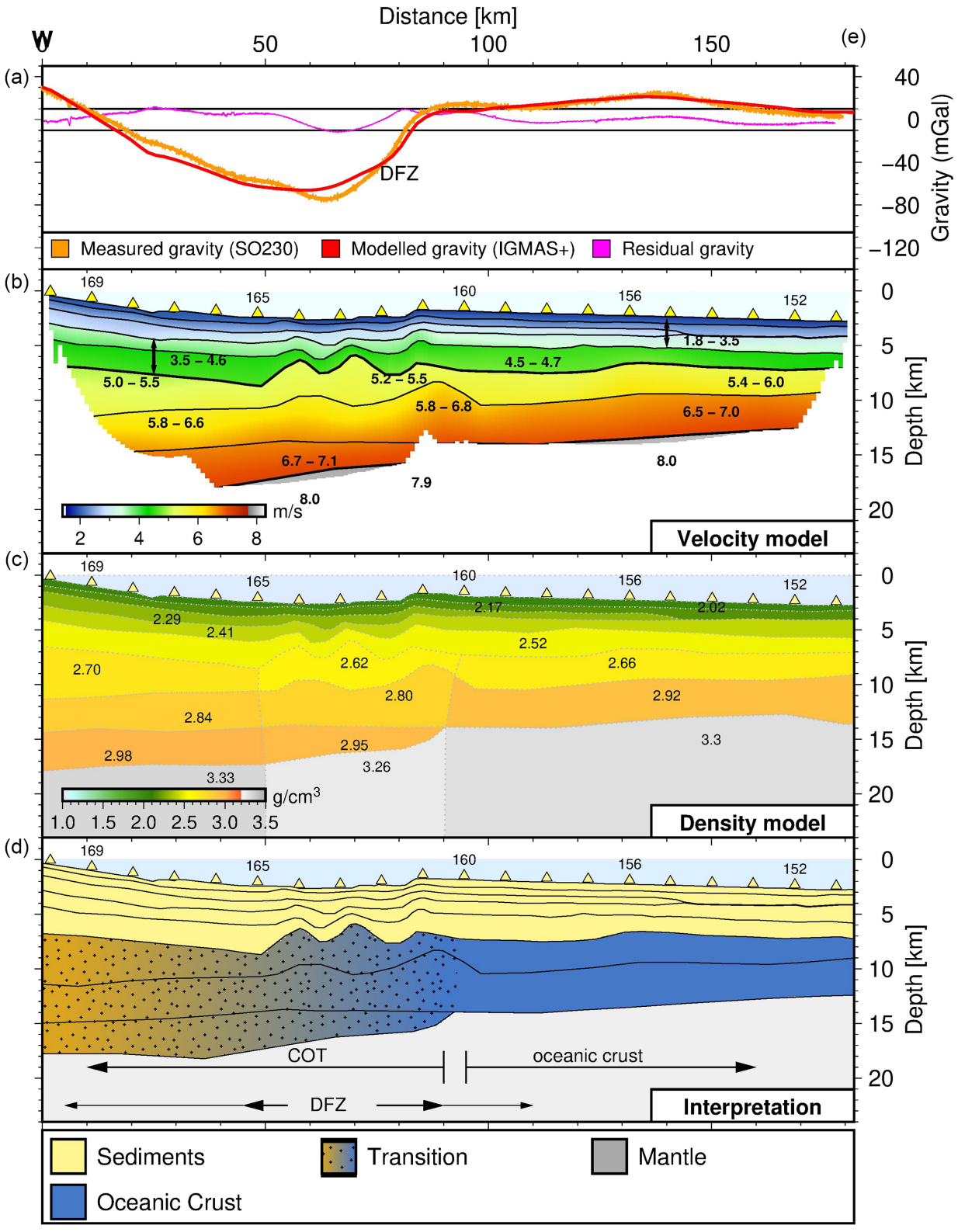

Figure 14. Gravity data, velocity and density model for profile AWI-20140150: (a) measured, calculated and residual gravity, (b) *P*-wave velocity model, only areas which are covered by rays are shown, (c) density model, (d) interpretation of the model. Yellow triangles indicate the OBS/OBH positions.

with reasonable signal-to-noise ratio that allow us to constrain its velocity to 8 km s^{-1} by amplitude modelling. The mantle at the eastern end of the line is modelled with a density of 3.3 g cm^{-3}.

5.2 Line AWI-20140130 (southern profile)

Profile AWI-20140130 crosses the southern end of the Kerimbas Basin at 13°S from east to west. The velocity model consists of

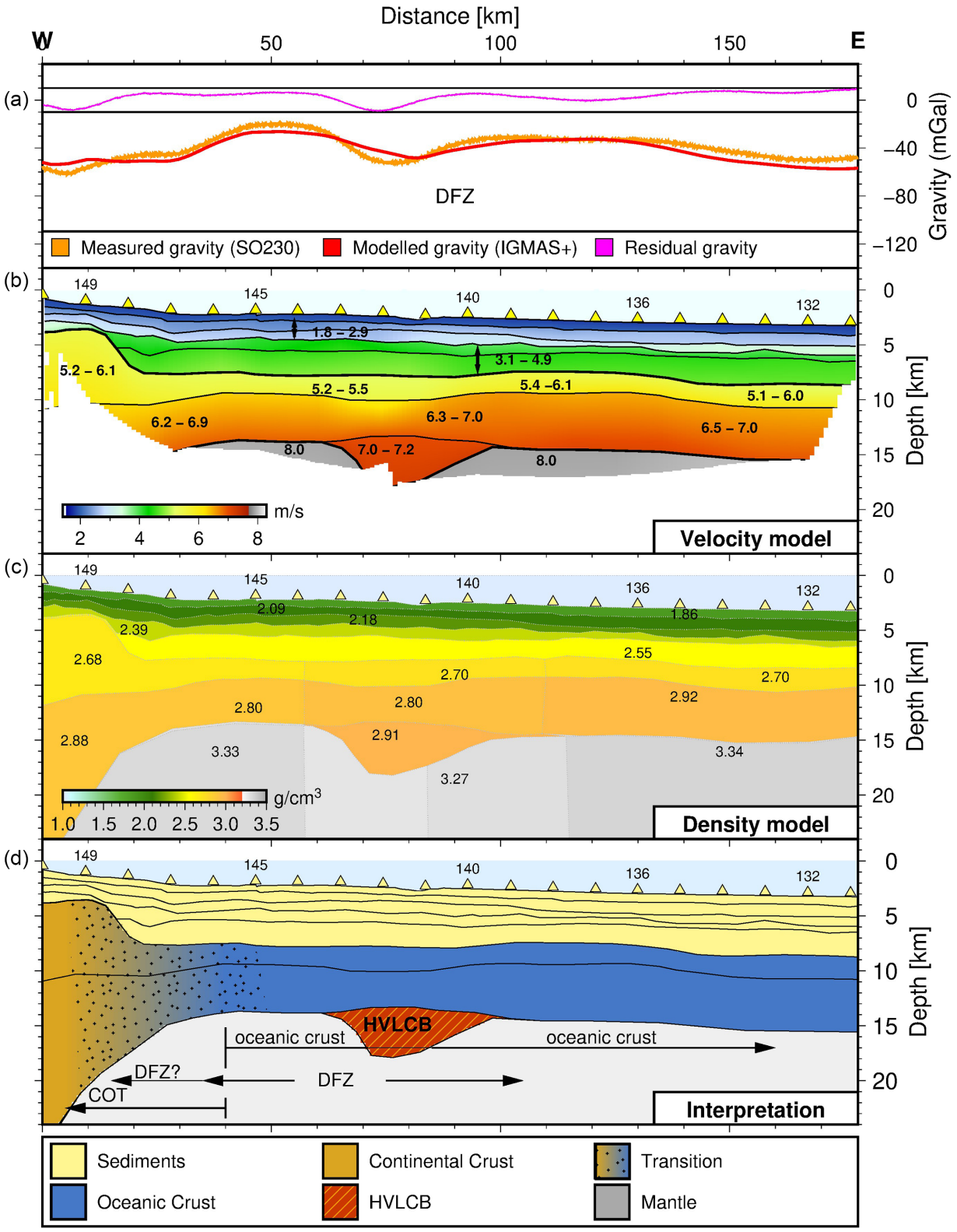

Figure 15. Gravity data, velocity and density model for profile AWI-20140130: a) measured, calculated and residual gravity b) *P*-wave velocity model, only areas which are covered by rays are shown, c) density model d) interpretation of the model. The dots indicate the COT. The yellow triangles indicate the OBS/OBH positions.

eight velocity layers, of which five are sedimentary layers; two crustal layers and one layer defines a bulge-shaped body of high velocities in the lower crust (Fig. 15; HVLCB). Additional layers are used for the water column and mantle. At the western end of the profile, near the Mozambican coast, the water depth is 800 m, and descends to 2250 m by km 30. Beyond this, the water depth

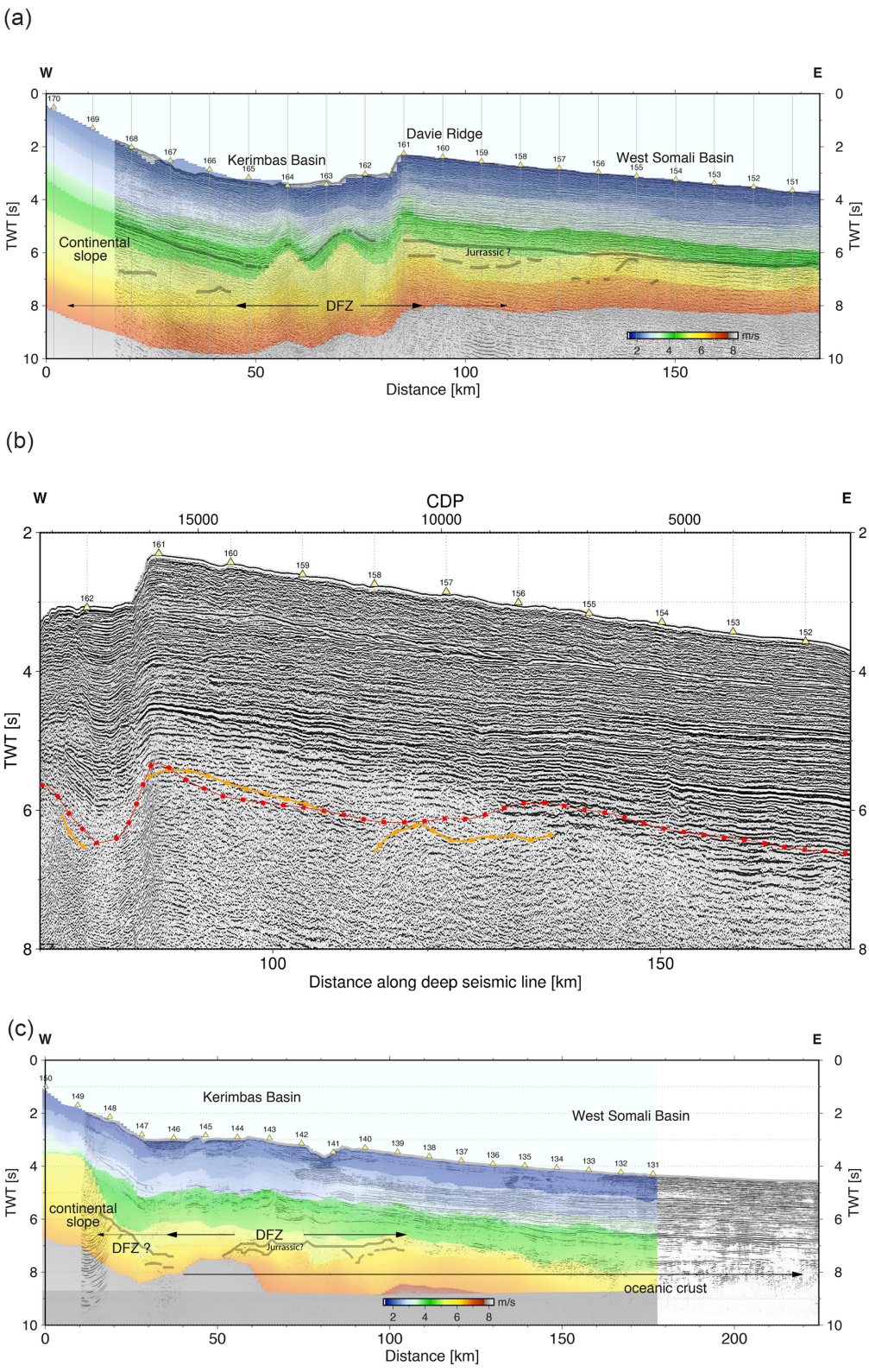

Figure 16. Showing seismic reflection data overlain by *P*-wave velocities derived from our wide-angle data. (a) AWI-20140150, please note that the both data sets could not be acquired coincidently because of ongoing industry seismic data acquisition during our experiment. Thus, both profiles are shifted by 2 km, (b) enlarged part in TWT of the above line showing more detailed information on the sediments below the eastern margin of the Kerimbas Basin. The weak basement reflections are marked by yellow lines. Red line indicates the approximate basement derived from our deep seismic line displaced northwards by 2 km and (c) AWI-20140130 is transferred into two way travel time and plotted on the parallel-acquired seismic reflection line. The grey line marks the picked Jurassic sediments and basement [Klimke & Franke 2016 (a); Franke *et al.* 2015 (b)]. The yellow triangles indicate the OBS/OBH positions on all panels.

gradually deepens to a deepest point at 3270 m at the eastern end of the profile, near the Comoros islands. Between km 77 and 87, a 10 km wide channel cuts into the uppermost sediments (Figs 15 and 16b). The suggested DR has no topography along this line. At km 70 (Fig. 15) the overall negative gravity reaches a local minimum of almost −60 mGal in absolute values. This low might mark the northernmost rim of a larger positive anomaly that is centred on Paisley Seamount (Fig. 1b).

The velocities in the sediments range from 1.7 to 4.6 km s^{-1} (Fig. 15, Table 4). East of the shelf break, a major velocity increase is observed between layers 3 and 4. The velocity in the western part abruptly increases from 2.9 to 3.9 km s^{-1} up to km 110, towards the east the velocity increases from 3.4 to 3.9 km s^{-1}. The thickness of sediments increases rapidly at the shelf break (km 20–30) from 2.5 to 4.5 km. Towards the east of the shelf break, within the Kerimbas Basin, the average thickness of the sediments is 4.5–6.5 km (Fig. 15; km 30–178). The basement topography is smooth and shows only a modest relief of up to 500 m, except near the shelf break (Fig. 15; km 30). The sediment layers are modelled with densities of 1.86–2.55 g cm^{-3} (Table 4; Fig. 15c).

In the western part (km 0–60), the upper crustal layer starts with a velocity of 5.3–5.7 km s^{-1}, which increases up to 6.1 km s^{-1}. The second crustal layer has velocities of 6.2–6.9 km s^{-1}. The thickness of the upper layer decreases from 6.7 km (km 5) to 1.6 km (km 60), and displays quite variable velocity gradients ranging from 0.31 to 0.09 s^{-1}. The westernmost 30 km of the lower crust has no ray coverage (Fig. 12). A maximum lower crustal thickness of 5 km is observed at km 30. The density modelling suggests that the entire crust at km 0 is about 15 km thick, assuming a lower crustal density of 2.88 g cm^{-3}. The density assigned to the upper crust is 2.68 g cm^{-3}. The mantle is modelled with a velocity of 8 km s^{-1} and a density of 3.33 g cm^{-3} (Table 3; Fig. 15; km 0–60).

The middle part of the profile (km 60–110) crosses the suggested prolongation of the DR (Fig. 1). Velocities of 5.2–5.4 km s^{-1}, which increase up to 5.8 km s^{-1}, are characteristic of the thin (1.7–2.9 km thick) upper crustal layer of the profile. The second layer shows velocities between 6.3 and 6.8 km s^{-1}, and has a thickness of 2.6–3.9 km. Velocity gradients are 0.13–0.28 s^{-1} in the upper crust, and 0.06–0.19 s^{-1} in the lower crust. Centred at km 74, the lower crustal layer is underlain by a bulge-shaped body with a width of 50 km and maximum thickness of 3.8 km (Fig. 15). We refer to this feature as a High Velocity Lower Crustal Body (HVCLB). Velocities assigned to the HVLCB range between 7.0 and 7.2 km s^{-1}, but are uncertain since the HVLCB is mapped only by reflected phases. However, the presence of the HVLCB has been confirmed by modelling synthetic seismograms (e.g. for OBS 143, Fig. 9). The density modelling is performed with an upper and lower crustal density of 2.7 and 2.9 g cm^{-3} (Fig. 15; Table 4). The assigned density in the up to 3.8 km thick HVLCB is 2.91 g cm^{-3}. The velocity of the mantle is lower (7.8 km s^{-1}) beneath the HVLCB than on the rest of the profile and its assigned density of 3.27 g cm^{-3} is less than that in the adjacent mantle (3.33–3.34 g cm^{-3}). The HVLCB is not associated with any topography in the crustal layers or sediments.

In the eastern part of the profile towards the Comoros islands (km 110 onwards), velocities between 5.1 and 6.1 km s^{-1} dominate the up-to 2.2 km thick upper crust. The underlying crustal layer has a thickness of 3.4–5.3 km, and velocities of 6.4–7.0 km s^{-1}. These values are typical of layers 2 and 3 in oceanic crust worldwide. The velocity gradients range between 0.25 and 0.51 s^{-1} in oceanic layer 2 and are significantly lower in oceanic layer 3 (0.11 and 0.15 s^{-1}). The assigned densities are 2.7 g cm^{-3} in the upper and 2.92 g cm^{-3} in the lower crust. The mantle has a velocity of 8 km s^{-1} and the assigned density is 3.34 g cm^{-3} (Fig. 15; Table 4).

6 INTERPRETATION AND DISCUSSION

To define crustal domains, along our profiles, we compare velocity depth functions along the profiles to global compilations for oceanic (White *et al.* 1992) and continental crust (Christensen & Mooney 1995). The compilations are made using data from undisputed continental and oceanic regions, and reveal that oceanic and continental crust have consistent and clearly distinguishable typical velocity gradients and crustal thicknesses. Along rifted margins the crustal fabric of the so-called continent–ocean transition zones (COTs) or transitional crust between unstretched continental crust and truly oceanic crust with seafloor spreading anomalies (White *et al.* 1992) cannot be interpreted with confidence using seismic data alone. Velocity–depth functions from deep seismic sounding models, in contrast, reveal COTs to be distinguishable by resembling neither continental nor oceanic archetypes. COT crust is thicker than normal oceanic crust, and has a velocity gradient more similar to that of continental than oceanic crust. For example, the interpretation of heavily intruded stretched continental crust is based on high seismic velocities in the lower crust within the COT (Sibuet *et al.* 2016). Despite this, it remains difficult on any given COT profile to determine (i) the seaward extent of stretched continental crust, (ii) the degree of continental intrusion by dense mantle-derived melt, (iii) the presence and extent of exhumed mantle material (Chian *et al.* 1999) and (iv) the extent of small basins floored by oceanic crust at unstable or short-lived mid-ocean ridge segments. Globally, insufficient drilling information is available to provide strong constraints on COT composition and/or variability.

As well as to global continental and oceanic crustal compilations, we also compare our velocity depth functions to those of deep seismic models crossing the adjacent Mozambique Basin and Channel (Leinweber *et al.* 2013; Müller *et al.* 2016; Müller & Jokat 2017; Vormann *et al.* 2020) to classify crustal domains in our study.

6.1 Central Kerimbas Basin

The northern profile AWI-20140150 (Fig. 14) crosses the central part of the Kerimbas Basin at 11.5°S.

The westernmost part of the profile (km 0–105), shows a complex velocity structure, which neither fits to stretched continental crust (Christensen & Mooney 1995) nor to normal oceanic crust (White *et al.* 1992; Fig. 17a1). The velocity gradient in the lower crust is higher than in typical stretched continental crust (Christensen & Mooney 1995). The velocity–depth functions closely resemble to those of intruded lower continental crust in the COT in the Bay of Bengal (Sibuet *et al.* 2016; Fig. 17a1), transitional crust off Morroco (Biari *et al.* 2016) and of stretched and intruded continental crust off western Madagascar (Vormann *et al.* 2020). The thickness of the observed crust is close to the smallest extent described by those authors. From these comparisons we classify the westernmost part of the line (km 0–105) as a COT comprised of highly stretched continental/transitional crust with lower crustal intrusions beneath the Kerimbas Basin.

We consider it unlikely that the COT hosts significant areas of exhumed oceanic or continental mantle. The vertical velocity gradients for exhumed mantle both in oceanic crust and within the COT

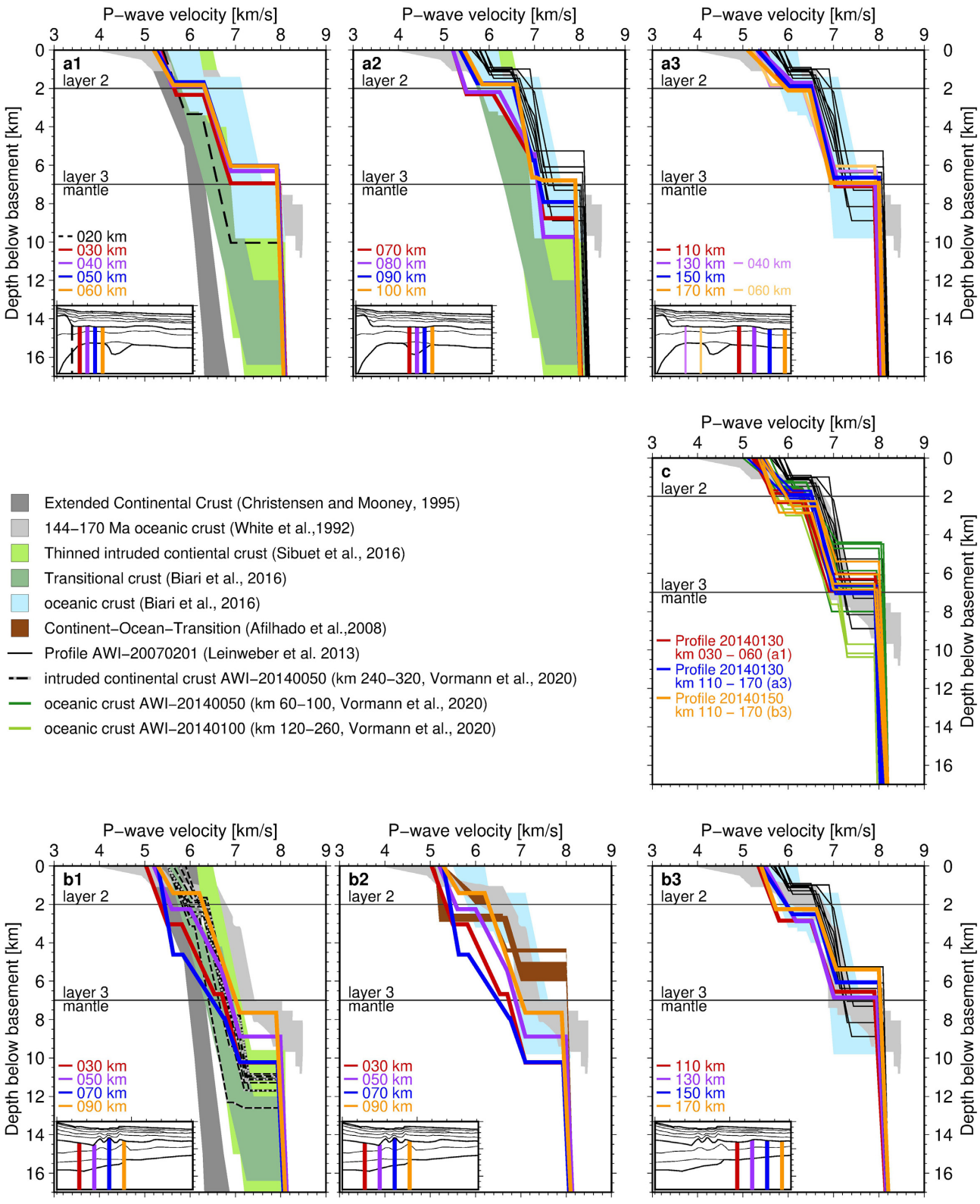

Figure 17. The velocity depth functions of several sections characterizing the different crustal domains along the profile AWI-20140150 (a1–a3) and AWI-20140130 (b1–b3) and the comparison of oceanic crust of both profiles with oceanic crust of adjacent profiles (Vormann *et al.* 2020) showing their distinct similarity (c). The sections are sorted into oceanic (White *et al.* 1992) and rifted continental crust (Christensen & Mooney 1995) and are additionally compared with velocity depth profiles of nearby lines in the Mozambique Basin from Leinweber *et al.* (2013), as well as a 1-D velocity–depth function of different types of transitional crust: intruded continental crust from Sibuet *et al.* (2016), COT from Afilhado *et al.* (2008) and exhumed mantle from Chian *et al.* (1999).

are higher, and the crust thinner (Chian *et al.* 1999; Afilhado *et al.* 2008) in COTs with extensive exhumation than we observe beneath the Kerimbas Basin (Fig. 17a2).

The density modelling (Fig. 14) matches the general trends in the observed gravity, but fails to reproduce the strong (100 mGal) gravity low above the Kerimbas Basin without arbitrarily reducing the density in the lower crust and the upper mantle.

Sinha *et al.* (2019) also report difficulties fitting the observed gravity data offshore southern Tanzania (Fig. 1b; line P1 at approx 7.5°S) with their initial crustal model based on seismic reflection data only. Without any additional control on crustal fabric from wide-angle data, they balanced their model by the addition of denser volcanic material beneath the oceanic crust off Tanzania (which starts approximately 50 km off the coast). A gravimetric model with extended continental crust beneath their line requires a COT of 400 km width. The authors dismissed this possibility because of the mainly transform margin architecture, but did not discuss a combined solution with partly extended continental crust.

In the eastern part of the profile (km 105–182), good resolution and ray coverage (Figs 11 and 13a) provides a velocity–depth distribution with a strong resemblance to that of oceanic crust (Biari *et al.* 2016; White *et al.* 1992; Fig. 17a3). Comparison with profiles south of our research area (Leinweber *et al.* 2013; Müller *et al.* 2016; Müller & Jokat 2017; Vormann *et al.* 2020; profile AWI-20140130) shows that the high velocities at the upper boundary of oceanic layer 2 are typical for this region (Figs 17a3 and c). Similarly, the density values are typical of oceanic crust observed in this region (Leinweber *et al.* 2013; Müller *et al.* 2016). The overall thickness of the crust varies between 4.9 and 6.5 km, thinner than the range of normal oceanic crust (7.1 ± 0.8 km; White *et al.* 1992). Magnetic measurements along the oceanic part of the northern profile show no distinct magnetic spreading anomalies. The seafloor here possibly formed during the Jurassic Quiet period, which is associated with rapid polarity changes and low field strength that impart little observable magnetic variability to its oceanic crust (e.g. Tivey *et al.* 2006). Further, the complex opening history of the West Somali Basin along the DFZ may have led to later tectonic disruption and deep (7–13 km; Sinha *et al.* 2019) burial of the Jurassic magnetic source layer. We interpret the eastern part of the profile (Fig. 14; >km 105) to image oceanic crust.

Our crustal classifications are in strong contrast to interpretations of Klimke & Franke (2016), who propose the entire profile to be underlain by extended continental crust, based on the complex reflection pattern of the shallow basement in their seismic reflection data (Fig. 16). Our seismic refraction data reveal the presence of thin (4.9 to 6.5 km) crust with velocities and densities typical for oceanic crust (Figs 14c, 17a3 and c). According to our interpretation, the basement reflection pattern observed by Klimke & Franke (2016) is a consequence of tectonic alteration of the oceanic basement by strike-slip faulting, possibly related to the action of the DFZ. Sauter *et al.* (2018) published a similar interpretation for the oceanic basement of Tanzania, in the northern part of the West Somali Basin. Our interpretation of the onset of oceanic crust or COB accords with that identified on reflection profile P3 (Figs 1 and 18; approx. at 10.6°S,) by Sinha *et al.* (2019). Our data reveal no strong or sharp variations in Moho depths beneath the Kerimbas Basin and adjacent oceanic crust. The velocity gradients and crustal thickness are not consistent with the existence of extensive areas of exhumed mantle.

6.2 Southern Kerimbas Basin

On the southern profile AWI-20140130 (Figs 15 and 17b), the crust rapidly thins from 20 km to 5 km thickness between km 0 and 40. The westernmost part of the profile has no raycoverage (Fig. 12), and thus, its crustal thickness is mostly based on the density model (Fig. 15). The increasing thickness and the close proximity to the African continent makes a change in the crustal structure likely. The upper part of the velocity depth function at km 20 (Fig. 17b1, dashed black) bears little resemblance to those of normal oceanic or continental crust (Christensen & Mooney 1995; White *et al.* 1992). But is similar to the highly intruded stretched continental crust of the Bay of Bengal (Sibuet *et al.* 2016) and the COT offshore Morocco (Biari *et al.* 2016). Based on this, we suggest that the COT west of km 30 consists of highly intruded and stretched continental crust. Eastwards, the velocity–depth profiles between km 30 and 60 are similar to those of normal oceanic crust (Fig. 17b1; Biari *et al.* 2016; White *et al.* 1992). The 2.5-D gravity modelling (Fig. 15c) suggests that densities are much like those on profiles across the southern Mozambican Margin: 2.69–2.91 g cm^{-3} (Leinweber *et al.* 2013; AWI-20070201, AWI-20070202, central Mozambique); 2.64–2.94 g cm^{-3} (Müller *et al.* 2016; AWI-20140010, Beira High); 2.7–2.91 g cm^{-3} (Vormann *et al.* 2020; AWI-20140050, AWI-20140100, Mozambique Channel).

The velocity depth distribution between km 60 and 110 remains more or less constantly similar to one of typical oceanic crust. The velocity gradient for oceanic layer 2 in our profile is slightly less steep than in White *et al.* (1992), but still a fit to oceanic crust (Biari *et al.* 2016). East of km 110, velocities of 5.3–5.5 km s^{-1} are observed in oceanic layer 2. These velocities are quite high but, as noted above, seem to be typical for the East African margin, north of 25°S (e.g. Leinweber *et al.* 2013; Müller *et al.* 2016; Müller & Jokat 2017; Vormann *et al.* 2020; 5.1–5.6 km s^{-1}; black lines in Fig. 17b3). Consistent with this, old sonobuoy measurements further north in the Somali Basin at 3°S (Fig. 1; Francis *et al.* 1966; Coffin *et al.* 1986) reveal seismic velocities of between 4.8 and 5.28 km s^{-1} at the top of oceanic layer 2. The comparison with oceanic crust of the southern West Somali Basin 170 km to the south reveals a close fit (Fig. 17c, AWI-20140100; Vormann *et al.* 2020). Another profile further south revealed oceanic crust from the Mozambique Basin, which is slightly thicker. The velocity distribution is also similar to the oceanic crust between km 40 and 60 (Fig. 17b3). The top of oceanic layer 3 is well determined along our profile with velocities of 6.4 km s^{-1}.

Between km 60 and 110, the data indicate underplated magmatic material or an HVLCB with velocities of 7.0–7.2 km s^{-1}. Observed crustal diffractions at many stations (Figs 5 and 7; OBS 137–141) indicate steep layer topography at km 60 (Fig. 15). The HVLCB is associated with a local, relative gravity minimum of around −40 mGal (Fig. 15a; absolute values range between −20 and −60 mGal). No basement or seafloor topography attributable to a continuation of the DR is observed, consistent with a change in its orientation from N–S to NW–SE just south of our line. The HVLCB is mapped by few PmP-arrivals and several diffractions, meaning its velocity can only be roughly estimated on the basis of amplitude modelling with OBS 143 data (Fig. 9). Further support for the existence and geometry of the HVLCB is provided by gravity modelling. The gravity data cannot be modelled satisfactorily without introducing a denser and thicker crust (8 km thick at maximum) than the surrounding oceanic crust for approximately 50 km (Fig. 15; km 60–110).

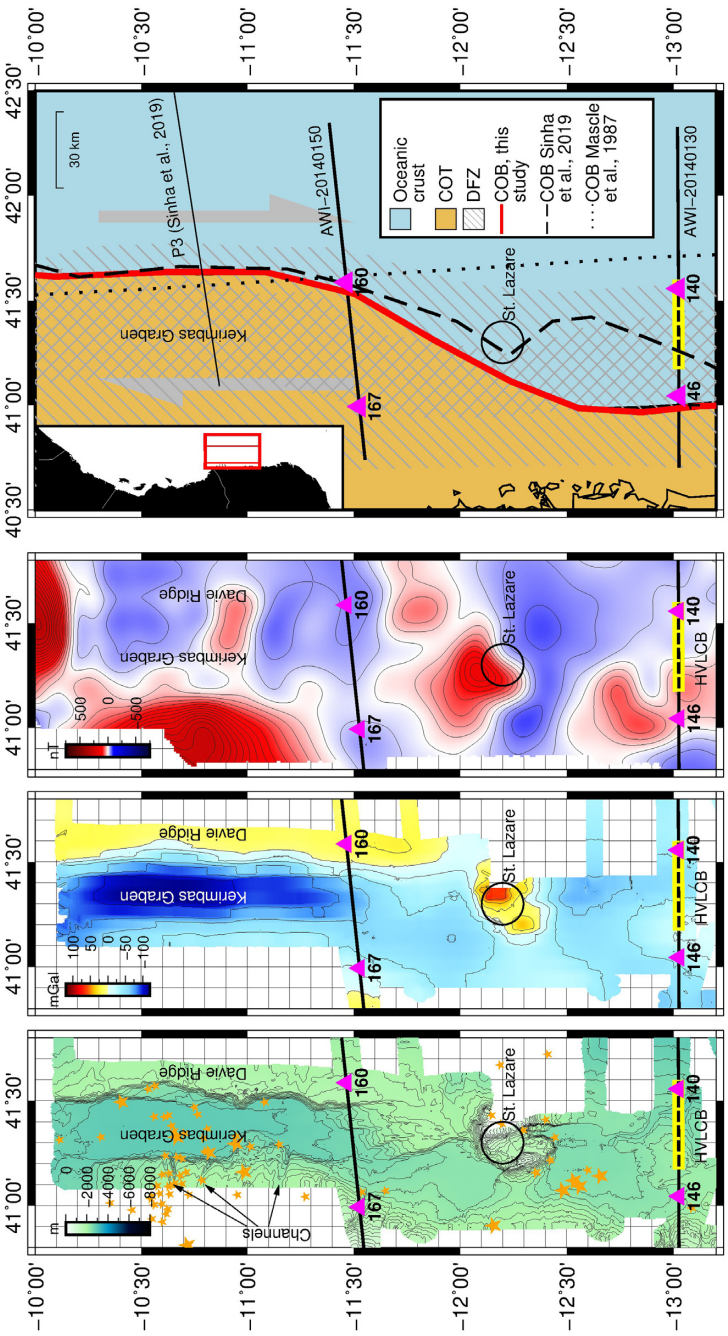

Figure 18. Regional geophysical data sets/results gathered in the research area during two consecutive RV Sonne cruises SO230 and SO231 (Jokat 2014; Franke *et al.* 2015). (a) Swath bathymetry and earthquake epicentres (orange stars, USGS earthquake catalogue), (b) shipborne gravity data and (c) compiled magnetic data acquired in the Kerimbas Basin, and (d) the location of the COT/COB derived from the seismic refraction data in the Kerimbas Basin research area. The pink triangle indicate selected OBS positions, the black lines represent the seismic refraction profiles presented in this study. The position of the HVLCB along the southern profile is marked with yellow in each panel.

Above the HVLCB (50 km wide, maximum 3.8 km thick), we observe a flat basement. Thus, it does not inflict an isostatic compensation yet. Franke *et al.* (2015) report numerous normal faults related to diffuse extension of the Kerimbas Basin above the HVLCB and towards the Mozambican coast. We assume that the HVLCB is likely to be a young feature related to this extension. The gravity high related to the Paisley Seamount (41.5°E, 14°S, 117 km in shortest distance; Fig. 1b) may extend towards the HVLCB, which might represent an underplate of the same magmatic mantle material that fed the growth of the Paisley Seamount. It is not possible to estimate of the size and extent of the underplated material on the basis of one profile alone. Below it, the mantle has a lower velocity (7.8 km s^{-1}) than the surrounding mantle (8.0 km s^{-1}) as well as a lower density (3.27 g cm^{-3} compared to 3.33 g cm^{-3}), which might be related to higher mantle temperatures (Mjelde *et al.* 2002). In brief, the tectonic relevance of the HVLCB cannot be resolved by our data and, thus, its interpretation remains speculative.

In summary, the crustal thickness of 6.5–7.5 km along AWI-20140130 is within the global average range for normal oceanic crust (7.1 ± 0.8 km; White *et al.* 1992). We attribute

the absence of observable magnetic reversal isochrons along the line to similar factors as their absence further north on AWI-20140150.

The seismic reflection data parallel to the wide-angle profile (Franke *et al.* 2015; Fig. 16c) do not permit a classification of the crustal structure. Instead, these data image the presence of numerous normal faults related to diffuse extension during formation of the Kerimbas Basin. These faults are located in the crust above the HVLCB and westwards towards the Mozambican coast. They are not resolvable with wide-angle seismic data.

The lowermost sedimentary layer on both profiles has high velocities of up to 4.8 km s^{-1}. Velocities like these are also characteristic for oceanic layer 2 (White *et al.* 1992). Such velocities however seem to be typical for the oldest sediments along the Mozambican and Tanzanian coasts. Numerous studies report sediment velocities of up to 4.9 km s^{-1} just above the acoustic/oceanic basement (Lort *et al.* 1979; Coffin *et al.* 1986; Leinweber *et al.* 2013; Müller *et al.* 2016, 2017; Vormann *et al.* 2020).

6.3 Onset of oceanic crust (COB)

The COB defines the onset of oceanic crust, whereas the COT defines an area in which the transition from continental to oceanic crust takes place. The crustal fabric of the COT can only be speculated on as mention earlier. Globally, studies of COTs have shown that they might include exhumed mantle, highly intruded crust or hyperextended crust (Whitmarsh & Miles 1995; Sibuet & Tucholke 2013; Eagles *et al.* 2015).

In previous studies, the position of the onset of oceanic crust in our research area has been only roughly estimated from seismic reflection data (Figs 1 and 18) without incorporating wide-angle information and is still under discussion (Mougenot *et al.* 1986a; Mascle *et al.* 1987; Franke *et al.* 2015; Klimke *et al.* 2016; Sauter *et al.* 2016; Sauter *et al.* 2018; Sinha *et al.* 2019).

The COB of the northern profile (AWI-20140150) is located at 41.6°E, at the eastern rift shoulder of the Kerimbas Basin (Fig. 18d). This boundary correlates with the COB as determined by Sinha *et al.* (2019) (Fig. 1, P3), who interpret it beneath the ridge shoulder on a seismic line 100 km to the north. On the southern line (AWI-20140130) oceanic crust is found east of 41.1°E, even closer to the present-day coastline (Figs 1 and 18). Here, the COB proposed by Sinha *et al.* (2019) lies 40 km further east and would cross the centre of the HVLCB (Fig. 15, km 60–110), which is located beneath oceanic crust. Our COB lies about 60 km closer to the coast of northern Mozambique than that of Mascle *et al.* (1987).

The landward edge of the COT cannot be determined from our wide-angle seismic modelling, due to the absence of land stations. The density modelling suggests an entire width of the COT at the southern Kerimbas Basin of no more than 100 km, of which 40 km are imaged by the seismic refraction data. In contrast, a 105 km wide COT is imaged on the northern profile. Here, density modelling across the western end of the profile onshore Mozambique supports a full COT width of approximately 180 km. Based on these observations, the width of the COT nearly doubles over an N–S distance of only 160 km. Its large extent based on our data contrasts with a proposed narrow COT of only 10 km offshore Tanzania (Sinha *et al.* 2019) but is comparable to that of Sauter *et al.* (2018), who suggest a COT width of 110 km.

6.4 The Davie Fracture Zone

The existence of the DFZ in the southern Mozambique Channel and Mozambique Basin is well established from seismic reflection data and plate kinematic modelling (Coffin & Rabinowitz 1987; Davis *et al.* 2016; Phethean *et al.* 2016; Müller & Jokat 2019; Reeves 2014). Before our experiment however little was known about its crustal fabric and evolution of its proposed continuation in the northern Mozambique Channel and southern West Somali Basin.

On our northern profile, the main part of the suggested DFZ is located approximately between km 50 and 105 in stretched continental crust (Fig. 14). West of km 50, towards the coast, we observe normal mantle densities. The presence of a wide crustal necking zone (at least 100 km) and a tens-of-kilometres wide COT with diffuse margins is not, however, typical of major transform continental margins (Bird 2001, Lorenzo 1997). The exceptionally thin oceanic crust east of km 100 is consistent with an evolution by initial oblique spreading between short-offset transform faults. However, our data cannot rule out the presence of DFZ that formed by landwards relocation of the oblique plate boundary when the plate divergence direction later changed to north–south. Such an interpretation is consistent with the proposed principal deformation zone in transitional crust at 10.6°S by Sinha *et al.* (2019) further north.

On the southern profile, the thin oceanic crust between the COB and HVLCB (km 35–60) could be attributable to the presence of a narrow fracture zone. At the HVLCB itself (km 60–110), we observe lower velocities and densities in the upper mantle, which also could be attributed to serpentinization in a fracture zone setting. Assuming a linear decrease in mantle density due to increasing serpentinite presence, the reduced density might relate to the presence of 10 per cent serpentinite. However, the positions of both profiles crossing a neotectonic zone suggest a different or additional interpretation: that the reduced mantle density is the signature of warmer mantle material currently welling up passively beneath an extensional branch of the EARS. The presence of the HVLCB in association with the Paisley Seamount and the recent volcanic activity on Sakalaves Seamount (Courgeon *et al.* 2018) is consistent with this interpretation. The additional presence of a pre-existing weak and thin zone in the lithosphere, such as a narrow fracture zone, might however explain the recent focussing of tectonic activity and mantle upwelling in the Kerimbas Basin region.

In summary, the width of the proposed northward continuation of the DFZ beneath the Kerimbas Basin varies between 55 km and 100 km (Fig. 18). The crustal fabric along each of our two profiles gradually changes from stretched continental to oceanic crust. Neither of the profiles reveal any clear crustal structures that can be unequivocally attributed to the presence of a single major fracture zone. The most unusual features of the southern profile, its reduced upper mantle density and seismic velocities and associated HVLCB, are not uniquely interpretable in terms of fluid flow and serpentinization along a major oceanic fracture zone. Similarly, neither profile shows any evidence for extreme crustal thickness variations that might be expected as a result of transpressional and transtensional alteration of continental crust along a continent–ocean transform plate boundary zone. The DFZ in our research area is not a typical fracture or a typical transform margin, because it does not separate unclassified transitional crust from oceanic crust and lacks

several indications for transform margins, such as a steep decrease of the Moho depth, marginal ridges, strong variations in oceanic basement topography or a narrow COT (Lorenzo 1997; Bird 2001). Thus, the proposed northern continuation of the DFZ should be interpreted as a broad fault zone, that formed in a transtensional regime.

6.5 Evolution of the northern Mozambican margin

The extent and location of the DFZ has implications for the pre-breakup palaeo-position of Madagascar within Gondwana and the resulting opening scenarios. Our new data show that the northern Mozambican margin cannot be classified as a classical narrow sheared margin but instead as the site of a broad COT underlain by some areas of unusually dense lower crustal material and relatively slow upper mantle seismic velocities. We interpret these findings in terms of the plate kinematic model of Müller & Jokat (2019), which best explains them.

In Early Jurassic times and until 157.1 Ma, East Gondwana initially rifted in roughly NW–SE orientation with respect to Africa (Fig. 2; Müller & Jokat 2019). The orientation of the early seafloor spreading caused obliquely rifted margins in our research area. At the N–S orientated Northern Mozambican margin, seafloor spreading with an oblique angle of approximately 45°–55° continued until 157 Ma (Fig. 2; Müller & Jokat 2019; Vormann *et al.* 2020). The initial oblique spreading resulted in the formation of several closely spaced minor fracture zones, perhaps pre-conditioning the crust for an unusually wide DFZ or DTS to form. This period saw the creation of about 230 km of transitional or oceanic crust at the central Mozambican and northern Somalian margins (Leinweber *et al.* 2013). Projection to the intervening N-S trending Mozambican margin implies the presence of up to 130 km of transitional or oceanic crust (Vormann *et al.* 2020).

In a second phase at 157–144 Ma (Fig. 2), the direction of plate divergence between West and East Gondwana changed to N–S (in the present-day African reference frame), and remained so for the next 60 Ma (Davis *et al.* 2016; Müller & Jokat 2019). This directional change caused the development of the DFZ in the Mozambique Channel that remained active until the termination of the spreading in the West Somali Basin. This N–S movement and thus formation of the DFZ modified already existing stretched continental and oceanic crust lying 50–150 km off the coast, which formed in the first spreading phase (Fig. 2).

Following our interpretation, the northern Mozambican margin cannot be classified as a simple sheared margin. No sharp thinning of continental crust is observed (Bird 2001). The initial oblique seafloor spreading in the first phase formed a smooth COT with a continuous seaward crustal thinning of continental crust. Neither the crust within the COT nor the adjacent oceanic crust shows strong basement or crustal thickness variations typical for shear and/or fracture zones. No evidence for any compression are found along the Northern Mozambican Margin. Most likely transtensional movements formed a broad fracture/fault zone without a sharp and defined extent in the West Somali Basin. Our seismic refraction data cannot put new constraints on the landward/seaward extent of the DFZ. For a detailed description of the transtensional movement the current kinematic model of Müller & Jokat (2019) is too coarse and detailed information from the Somali Basin is lacking. Deep seismic data off Tanzania and Kenya are needed as well as systematic marine magnetic data in the Somali Basin are needed to validate or refine our interpretation.

Finally, the present-day distribution of seismicity in our research area reveals it to host an offshore branch of the EARS. In this setting, it is possible to envisage the presence of warm mantle material that is consistent with the observation of unusually slow upper mantle velocities of less than 8.0 km s^{-1} in narrow parts of both of our profiles. This interpretation is supported by a dredged 7 Myr old basaltic rocks recovered from the northern Mozambique Ridge, which has the same geochemical composition like similar rocks in the Afar region (O'Connor *et al.* 2019). It shows that 'superplume mantle exists beneath the rift the length of Africa from the Red Sea to the Indian Ocean offshore southern Mozambique' (O'Connor *et al.* 2019). In contrast, the lower crust above the 'hotter' upper mantle shows no indications for higher seismic velocities due to massive intrusions. If present the intrusions are not resolved by our experimental set-up

7 CONCLUSION

We provide new insight into the crustal fabric off northern Mozambique from seismic wide-angle data modelling. The oldest oceanic crust is found no more than 150 km offshore the Mozambican coast at about 41.1°E/13°S and 41.6°E/11.5°S. The COT is approx. 100 km wide on the southern profile and much broader (approx. 180 km) along the northern one. The proposed northward continuation of the DFZ lies in a zone that is at least 70 km wide from west to east, and overlaps with the margin's COT. The variable crustal structure of this zone and the varying width of the COT are interpreted to have developed during an early phase of oblique plate divergence accommodated first by continental extension, later by the formation of transitional crust, and later still (until 157 Ma) accretion of oceanic crust. Subsequently, during a second phase of seafloor spreading (Fig. 2) these features were overprinted and modified/faulted by the N-S directed movements between East and West Gondwana.

Localized underplating of the lower crust (HVLCB) is detected beneath the southern profile, at the northern edge of a gravity high that continues to the Paisley Seamount. The oceanic basement above the HVLCB is flat, and, thus, is not in isostatic equilibrium. We interpret the HVLCB as a young feature produced by partial melting of the same mantle material that is currently supplying melt to form the Paisley Seamount. The true size of the HVLCB remains speculative. Finally, we observe no evidence for major tectonic modification of the crust as part of the EARS. Instead, the strongest possible signal of the EARS comes in the form of slightly reduced upper mantle densities that may indicate ongoing upwelling of warm material beneath the rift zone.

ACKNOWLEDGEMENTS

This project was founded through a grant by the German Federal Ministry of Education and Research (BMBF 03G0230A and 03G0231A) and AWI internal funding. We thank Captain Detlef Korte and his Crew of RV Sonne for his support, the GEOMAR for providing the OBS/H-Stations, Jürgen Gossler for his support during the OBS deployment, Ingo Heyde and Bernd Schreckenberger (BGR) for the magnetic/gravity data acquisition. We thank Sabine Schmidt for her support with the IGMAS+ software. Graeme Eagles provided substantial comments to enhance the content and English language of the paper. Comments/suggestions from two reviewers, F. Klingelhoefer and S. Sinha, greatly enhanced the paper.

DATA AVAILABILITY

The data underlying this paper will be shared on reasonable request to the corresponding author.

REFERENCES

Afilhado, A., Matias, L., Shiobara, H., Hirn, A., Mendes-Victor, L. & Shimamura, H., 2008. From unthinned continent to ocean: the deep structure of the West Iberia passive continental margin at 38°N, *Tectonophysics,* **458**(1–4), 9–50.

Altenbernd, T., Jokat, W., Heyde, I. & Damm, V., 2014. A crustal model for northern Melville Bay, Baffin Bay, *J. geophys. Res.,* **119,** 8610–8632.

Bassias, Y., 1992. Petrological and geochemical investigation of rocks from the Davie fracture zone (Mozambique Channel) and some tectonic implications, *J. Afr. Earth Sci. (and Middle East),* **15,** 321–339.

Biari, Y. , Klingelhoefer, F. Sahabi, M. Aslanian, D. Schnurle, P. Berglar, K. Moulin, M. Mehdi, K. Graindorge, D. Evain, M. Benabdellouahed, M. & Reichert, C. 2015. Deep crustal structure of the North-West African margin from combined wide-angle and reflection seismic data (MIRROR seismic survey), *Tectonophysics,* 656 154–174. https://doi.org/10.1016/j.tecto.2015.06.019.

Bird, D., 2001. Shear margins: continent–ocean transform and fracture zone boundaries, *Lead. Edge,* **20,** 150. https://doi.org/10.1190/1.1438894

Bohlen, T. , De Nil, D. Daniel, K. Jetschny, S. Köhn, D. & Jetschny, S. 2016. SOFI2D -Seismic Modeling with Finite Differences 2D - Elastic and Viscoelastic Version - Users Guide, Software: https://git.scc.kit.edu/GPIAG-Software/SOFI2D; Manual: https://git.scc.kit.edu/GPIAG-Software/SOFI2D/uploads/3ac63892995d5d0e665f3eb1f416dc85/guide_sofi2D.pdf.

Bohlen, T., 1998. *Viskoelastische FD-Modellierung seismischer Wellen zur Interpretation gemessener Seismogramme,* Kiel.

Bohlen, T., 2002. Parallel 3-D viscoelastic finite difference seismic modelling, *Comput. Geosci.,* **28,** 887–899.

Brocher, T.M., 2008. Compressional and shear-wave velocity versus depth relations for common rock types in northern California, *Bull. seism. Soc. Am.,* **98,** 950–968.

Bunce, E.T., Langseth, M.G., Chase, R.L. & Ewing, M., 1967. Structure of the western Somali Basin, *J. geophys. Res.,* **72,** 2547–2555.

Bunce, E.T. & Molnar, P., 1977. Seismic reflection profiling and basement topography in the Somali Basin: possible fracture zones between Madagascar and Africa, *J. geophys. Res.,* **82,** 5305–5311.

Chian, D., Louden, K.E., Minshull, T.A. & Whitmarsh, E.B., 1999. Deep structure of the ocean-continent transition in the southern Iberia Abyssal Plain from seismic refrac tion profiles: ocean Drilling Program (Legs 149 and 173) transect, *J. geophys. Res.,* **104**(B4), 7443–7462.

Chorowicz, J., 2005. The East African rift system, *J. Afr. Earth Sci.,* **43,** 379–410.

Christensen, N.I. & Mooney, W.D., 1995. Seismic velocity structure and composition of the continental crust: a global view, *J. geophys. Res.,* **100,** 9761. https://doi.org/10.1029/95JB00259

Cochran, J.R., 1988. Somali Basin, Chain Ridge, and origin of the northern somali basin gravity and geoid low, *J. geophys. Res.,* **93,** 11985–12 008.

Coffin, M.F. & Rabinowitz, P.D., 1987. Reconstruction of Madagascar and Africa: evidence from the Davie Fracture Zone and Western Somali Basin, *J. Geophys. Res.,* **92,** 9385. https://doi.org/10.1029/JB092iB09p09385

Coffin, M.F., Rabinowitz, P.D. & Houtz, R.E., 1986. Crustal structure in the Western Somali Basin, *Geophys. J. R. astr. Soc.,* **86,** 331–369.

Courgeon, S. *et al.* 2018. The offshore east African rift system: new insights from the Sakalaves seamounts (Davie Ridge, SW Indian Ocean), *Terra Nova,* **30,** 380–388.

Cox, K.G., 1992. Karoo igneous activity, and the early stages of the break-up of Gondwanaland, *Geol. Soc. London, Spec. Publ.,* **68,** 137–148.

Davis, J.K., Lawver, L.A., Norton, I.O. & Gahagan, L.M., 2016. New Somali Basin magnetic anomalies and a plate model for the early Indian Ocean, *Gondwana Res.*, **34,** 16–28.

Déprez, A., Doubre, C., Masson, F. & Ulrich, P., 2013. Seismic and aseismic deformation along the East African Rift System from a reanalysis of the GPS velocity field of Africa, *Geophys. J. Int.,* **193,** 1353–1369.

Eagles, G. & König, M., 2008. A model of plate kinematics in Gondwana breakup, *Geophys. J. Int.,* **173,** 703–717.

Eagles, G., Pérez-Díaz, L. & Scarselli, N., 2015. Getting over continent ocean boundaries, *Earth-Sci. Rev.*, **151,** 244–265. https://doi.org/10.1016/j.earscirev.2015.10.009.

Emerick, C.M. & Duncan, R.A., 1982. Age progressive volcanism in the Comores Archipelago, western Indian Ocean and implications for Somali plate tectonics, *Earth planet. Sci. Lett.,* **62,** 415–428.

Francis, T.J.G., Davies, D. & Hill, M.N., 1966. Crustal structure between Kenya and the Seychelles, *Phil. Trans. R. Soc. A,* **259,** 240–261.

Franke, D. *et al.* 2015. The offshore East African Rift System: structural framework at the toe of a juvenile rift, *Tectonics,* **34,** 2086–2104.

Fromm, T., 2016. PRay - a graphical user interface for interactive visualization and modification of rayinvr models, *J. Appl. Geophys.,* **124,** 1–3.

Gaina, C., Torsvik, T.H., van Hinsbergen, D.J.J.J., Medvedev, S., Werner, S.C. & Labails, C., 2013. The African plate: a history of oceanic crust accretion and subduction since the Jurassic, *Tectonophysics,* **604,** 4–25.

Gardner, G.H.F. , Gardner, L.W. & Gregory, A.R. 1974. Formation velocity and density - the diagnostic basics for stratigraphic traps, *Geophysics,* **39,**(770–780. https://doi.org/10.1190/1.1440465.

GEBCO, 2014. *International Hydrographic Organization (IHO) and the Intergovernmental Oceanographic Commission (IOC) of UNESCO,* URL http://www.gebco.net.

Geiger, M., Clark, N.D. & Mette, W., 2004. Reappraisal of the timing of the breakup of Gondwana based on sedimentological and seismic evidence from the Morondava Basin, Madagascar, *J. Afr. Earth Sci.,* **38,** 363–381.

Götze, H.-J.-J. & Lahmeyer, B., 1988. Application of three-dimensional interactive modeling in gravity and magnetics, *Geophysics,* **53,** 1096–1108. https://doi.org/10.1190/1.1442546

Götze, H.-J., 2007. *IGMAS+, Interactive Geophysical Modelling Assistant,* v1.1.1892.1, Transinsight GmbH.

Grantham, G.H., Maboko, M. & Eglington, B.M., 2003. A review of the evolution of the Mozambique Belt and implications for the amalgamation and dispersal of Rodinia and Gondwana, *Geol. Soc. London, Spec. Publ.*, **206,** 401–425.

Heirtzler, J.R. & Burroughs, R.H., 1971. Madagascar's paleoposition: new data from the Mozambique Channel, *Science ,* **174,** 488–490.

Jokat, W., 2014. *The Expedition of the Research Vessel "Sonne" to the Mozambique Basin in 2014 (SO230),* Berichte zur Polar- und Meeresforschung.

Jokat, W., Boebel, T., König, M. & Meyer, U., 2003. Timing and geometry of early Gondwana breakup, *J. geophys. Res.,* **108**. https://doi.org/10.1029/2002JB001802

Jokat, W. & Schmidt-Aursch, M.C., 2007. Geophysical characteristics of the ultraslow spreading Gakkel Ridge, Arctic Ocean, *Geophys. J. Int.,* **168,** 983–998.

Key, R.M., Smith, R.a., Smelror, M., Saether, O.M., Thorsnes, T., Powell, J.H., Njange, F. & Zandamela, E.B., 2008. Revised lithostratigraphy of the Mesozoic-Cenozoic succession of the onshore Rovuma Basin, northern coastal Mozambique, *South Afr. J. Geol.,* **111,** 89–108.

Klimke, J. & Franke, D., 2016. Gondwana breakup: no evidence for a Davie Fracture Zone offshore northern Mozambique, Tanzania and Kenya, *Terra Nov.*, **28,** 233–244.

Klimke, J., Franke, D., Gaedicke, C., Schreckenberger, B., Schnabel, M., Stollhofen, H., Rose, J. & Chaheire, M., 2016. How to identify oceanic crust—evidence for a complex break-up in the Mozambique Channel, off East Africa, *Tectonophysics,* **693,** 436–452. https://doi.org/10.1016/j.tecto.2015.10.012

Klimke, J., Franke, D., Mahanjane, E.S. & Leitchenkov, G., 2018. Tie points for Gondwana reconstructions from a structural interpretation of the Mozambique Basin, East Africa and the Riiser-Larsen Sea, Antarctica, *Solid Earth,* **9,** 25–37.

König, M. & Jokat, W., 2006. The Mesozoic breakup of the Weddell Sea, *J. geophys. Res.,* **111,** 1–28. https://doi.org/10.1029/2006JB004035

Lawver, L.A. *et al.* 1991. Evolution of the Antarctic continental margins, in *Proceedings of the 5th International Antarctic Earth Science Symposium,* pp. 533–539, Thomson M.R.A., Crame J.A., Thomson J.W. eds, Cambridge Univ. Press.

LeClaire, L., Bassias, Y., Clocchiatti, M. & Segoufin, J., 1989. La Ride de Davie dans le Canal de Mozambique : approche stratigraphique et géodynamique, *C. R. Acad. Sci.,* **308,** 1077–1082.

Leinweber, V.T. & Jokat, W., 2012. The Jurassic history of the Africa-Antarctica corridor - new constraints from magnetic data on the conjugate continental margins, *Tectonophysics,* **530–531,** 87–101.

Leinweber, V.T. *et al.* 2013. The crustal structure of the Central Mozambique continental margin—wide-angle seismic, gravity and magnetic study in the Mozambique Channel, Eastern Africa, *Tectonophysics,* **599,** 170–196.

Ljones, F., Kuwano, A., Mjelde, R., Breivik, A., Shimamura, H., Murai, Y. & Nishimura, Y., 2004. Crustal transect from the North Atlantic Knipovich Ridge to the Svalbard Margin west of Hornsund, *Tectonophysics,* **378,** 17–41.

Lorenzo, J.M., 1997. Sheared continent—ocean margins : an overview, *Geo-Marine Lett*., **17,** 1–3.

Lort, J.M., Limond, W.Q., Segoufin, J., Patriat, P., Delteil, J.R. & Damotte, B., 1979. New seismic data in the Mozambique Channel, *Mar. Geophys. Res.,* **4,** 71–89.

Macgregor, D., 2018. History of the development of Permian–Cretaceous rifts in East Africa: a series of interpreted maps through time, *Pet. Geosci.,* **24,** 8–20.

Mahanjane, E.S., 2012. A geotectonic history of the northern Mozambique Basin including the Beira High—a contribution for the understanding of its development, *Mar. Pet. Geol.,* **36,** 1–12.

Mahanjane, E.S., 2014. The Davie Fracture Zone and adjacent basins in the offshore Mozambique margin—a new insights for the hydrocarbon potential, *Mar. Pet. Geol.,* **57,** 561–571.

Mascle, J., Mougenot, D., & Blarez, E., 1987. African transform continental margins: examples from Guinea, the Ivory Coast and Mozambique, *Geol. J.,* **22,** 537–561.

Mjelde, R., Kasahara, J., Shimamura, H., Kamimura, A., Kanazawa, T., Kodaira, S., Raum, T. & Shiobara, H., 2002. Lower crustal seismic velocity-anomalies; magmatic underplating or serpentinized peridotite? Evidence from the Vøring Margin, NE Atlantic, *Mar. Geophys. Res.,* **23,** 169–183.

Morelli, C., Gantar, C., Honkasalo, T., McConnel, R.K., Tanner, J.G., Szabo, B., Uotila, U., & Whalen, C.T., 1974. The International Gravity Standardisation Net 1971 (IGSN71). Spec. Publ. No. 4.

Mougenot, D., Recq, M., Virlogeux, P., & Lepvrier, C., 1986a. Seaward extension of the East African Rift, *Nature,* **321,** 599–603.

Mougenot, D., Virlogeux, P., Vanney, J., & Malod, J., 1986b. La marge continentale au Nord du Mozambique: résultats préliminaires de la campagne md40 /macamo, *Bull. Soc. géol. Fr.,* **II,** 419–422.

Mulibo, G.D. & Nyblade, A.A., 2016. The seismotectonics of Southeastern Tanzania: implications for the propagation of the eastern branch of the East African Rift, *Tectonophysics,* **674,** 20–30. https://doi.org/10.1016/j.tecto.2016.02.009

Müller, C.O. & Jokat, W., 2017. Geophysical evidence for the crustal variation and distribution of magmatism along the central coast of Mozambique, *Tectonophysics,* **712–713,** 684–703.

Müller, C.O. & Jokat, W., 2019. The initial Gondwana break-up: a synthesis based on new potential field data of the Africa-Antarctica Corridor, *Tectonophysics,* **750,** 301–328.

Müller, C.O., Jokat, W. & Schreckenberger, B., 2016. The crustal structure of Beira High, central Mozambique—Combined investigation of wide-angle seismic and potential field data, *Tectonophysics,* **683,** 233–254.

Nafe, J.E. & Drake, C.L., 1957. Variation with depth in shallow and deep water marine sediments of porosity, density and the velocities of compressional and shear waves, *Geophysics,* **22,** 523–552. https://doi.org/10.1190/1.1438386

O'Connor, J.M., Jokat, W., Regelous, M., Kuiper, K.F., Miggins, D.P. & Koppers, A.A.P., 2019. Superplume mantle tracked isotopically the length of Africa from the Indian Ocean to the Red Sea, *Nat. Commun.,* **10,** 5493. https://doi.org/10.1038/s41467-019-13181-7

Ogg, J.G., 2012. Geomagnetic polarity time scale, *In: Gradstein, F.M., Ogg, J.G., Schmitz, M., Ogg, G. (Eds.), The Geologic Time Scale 2012. Elsevier,* 85–113. .

Phethean, J.J.J., Kalnins, L.M., van Hunen, J., Biffi, P.G., Davies, R.J. & McCaffrey, K.J.W., 2016. Madagascar's escape from Africa: a high-resolution plate reconstruction for the Western Somali Basin and implications for supercontinent dispersal, *Geochem. Geophys. Geosyst.,* **17,** 5036–5055.

Rabinowitz, P.D., 1971. Gravity Anomalies across the East African Continental Margin, *J. geophy. Res,* **76**(), 7107–7117. https://agupubs.onlinelibrary.wiley.com/doi/abs/10.1029/JB076i029p07107 .

Rabinowitz, P.D., Coffin, M.F. & Falvey, D., 1983. The separation of Madagascar and Africa, *Science*., **220**(4592), 67–69.

Reeves, C., 2014. The position of Madagascar within Gondwana and its movements during Gondwana dispersal, *J. Afr. Earth Sci.,* **94,** 45–57.

Reeves, C.V, 2018. The development of the East African margin during Jurassic and Lower Cretaceous times: a perspective from global tectonics, *Pet. Geosci.,* **24,** 41–56.

Sacchi, R., Cadoppi, P. & Costa, M., 2000. Pan-African reactivation of the Lurio segment of the Kibaran Belt system: a reappraisal from the recent age determinations in northern Mozambique, *J. Afr. Earth Sci.,* **30,** 629–639.

Salman, G. & Abdula, I., 1995. Development of the Mozambique and Ruvuma sedimentary basins, offshore Mozambique, *Sediment. Geol.,* **96,** 7–41.

Sandwell, D.T. *et al.* 2014. New global marine gravity model from CryoSat-2 and Jason-1 reveals buried tectonic structure, *Science,* **346,** 65–67.

Saria, E., Calais, E., Stamps, D.S., Delvaux, D. & Hartnady, C.J.H., 2014. Present-day kinematics of the East African Rift, *J. geophys. Res.,* **119**. https://doi.org/10.1002/2013JB010901

Sauter, D., Ringenbach, J.C., Cannat, M., Maurin, T., Manatschal, G. & McDermott, K.G., 2018. Intraplate deformation of oceanic crust in the West Somali Basin: insights from long-offset reflection seismic data, *Tectonics,* **37,** 588–603.

Sauter, D. *et al.* 2016. Evidence for magma entrapment below oceanic crust from deep seismic reflections in the western Somali basin, *Geology*. **44** (6), 407–410. https://doi.org/10.1130/G37747.1

Schlindwein, V., & Jokat, W, 1999. Structure and evolution of the continental crust of northern east Greenland from integrated geophysical studies., *J. Geophys. Research,* **104,** 15227–15245. https://doi.org/10.1029/1999JB900101.

Schmidt, S., Götze, H., Fichler, C., Ebbing, J. & Alvers, M.R., 2007. 3D Gravity, FTG and magnetic modeling : the new IGMAS + software, *EGM 2007 Int. Work.* 1–4.

Scrutton, R.a., 1978. Davie fracture zone and the movement of Madagascar, *Earth planet. Sci. Lett.,* **39,** 84–88.

Scrutton, R.a., Heptonstall, W.B., & Peacock, J.H., 1981. Constraints on the motion of Madagascar with respect to Africa, *Mar. Geol.,* **43,** 1–20.

Segoufin, J. & Patriat, P., 1980. Existence d'anomalies mesozoiques dans le bassin de somalie. implications pour les relations Afrique-Antarctique-Madagascar, *C. R. Acad. Sci.* 85–88.

Sibuet, J.C., Klingelhoefer, F., Huang, Y.P., Yeh, Y.C., Rangin, C., Lee, C.S. & Hsu, S.K., 2016. Thinned continental crust intruded by volcanics beneath the northern Bay of Bengal, *Mar. Pet. Geol.,* **77,** 471–486.

Sibuet, J.C. & Tucholke, B.E., 2013. The geodynamic province of transitional lithosphere adjacent to magma-poor continental margins, *Geo. Soc. Spec. Publ.,* **369**(1), 429–452

Sinha, S.T., Saha, S., Longacre, M., Basu, S., Jha, R. & Mondal, T., 2019. Crustal Architecture and nature of continental breakup along a transform margin: new insights from Tanzania–Mozambique Margin, *Tectonics,* 2018TC005221. https://doi.org/10.1029/2018TC005221

Smelror, M., Key, R.M., Smith, R.A. & Njange, F., 2008. Late Jurassic and Cretaceous palynostratigraphy of the onshore Rovuma Basin, Northern Mozambique, *Palynology,* **32,** 63–76.

Stamps, D.S., Calais, E., Saria, E., Hartnady, C., Nocquet, J.M., Ebinger, C.J. & Fernandes, R.M., 2008. A kinematic model for the East African Rift, *Geophys. Res. Lett.,* **35,** 1–6.

Stamps, D.S., Saria, E. & Kreemer, C., 2018. A Geodetic Strain Rate Model for the East African Rift System, *Sci. Rep.,* **8,** 1–8.

Stanca, R., Kearns, H., Paton, D., Hodgson, N., Rodriguez, K. & Hussein, A.A.(2016). Offshore Somalia: crustal structure and implications on thermal maturity, *First Break,* **34**(12), https://doi.org/10.3997/1365-2397.34.12.87305

Thompson, J.O., Moulin, M., Aslanian, D., de Clarens, P. & Guillocheau, F. 2019. New starting point of the Indian Ocean: second phase of breakup for Gondwana, *Earth Sci. Rev.,* **191,** 26–56.

Tivey, M.A., Sager, W.W., Lee, S. & Tominaga, M., 2006. Origin of the Pacific Jurassic quiet zone, *Geology,* **34,** 789. https://doi.org/10.1130/G22894.1

Tuck-Martin, A., Adam, J. & Eagles, G., 2018. New plate kinematic model and tectono-stratigraphic history of the East African and West Madagascan Margins, *Basin Res.,* **30,** 1118–1140.

Ueda, K. *et al.* 2012. Post-collisional high-grade metamorphism, orogenic col lapse and differential cooling of the East African Orogen of Northeast Mozambique, *J. Geol.,* **120,** 507–530.

Veeken, P.C.H. & Titov, K.V., 1996. Gravity modelling along a seismic line across the Mandawa basin, southeastern Tanzania, *J. Afr. Earth Sci.,* **22,** 207–217.

Virlogeux, P., 1987. *Geologie de la marge nord-Mozambique et de la chaine Davie (9° S à 21° S): campagne MD40-MACAMO, PhD thesis*. Universite Pierre et Marie Curie.

Vormann, M., Franke, D. & Jokat, W., 2020. The crustal structure of the southern Davie Ridge offshore northern Mozambique—a wide-angle seismic and potential field study, *Tectonophysics,* **778,** 228370. https://doi.org/10.1016/j.tecto.2020.228370.

White, R.S., McKenzie, D. & O'Nions, R.K., 1992. Oceanic crustal thickness from seismic measurements and rare earth element inversions, *J. geophys. Res.,* **97,** 19 683–19 715.

Whitmarsh, R.B. & Miles, P.R., 1995. Models of the development of the West Iberia rifted continental margin at 40°30'N deduced from surface and deep-tow magnetic anomalies, *J. geophys. Res.,* **100**(B3), 3789–3806.

Wopfner, H. & Kaaya, C.Z., 1991. Stratigraphy and morphotectonics of Karoo deposits of the northern Selous Basin, Tanzania, *Geol. Mag.,* **128**(4), 319–334.

Zelt, B.C., 2004. 'zp - Software for plotting wide-angle seismic data in SEGY format.' Available at: http://www.soest.hawaii.edu/users/bzelt/zp/zp.html

Zelt, C.A., 1999. Modelling strategies and model assessment for wide-angle seismic traveltime data, *Geophys. J. Int.,* **139,** 183–204.

Zelt, C.A. & Smith, R.B., 1992. Seismic traveltime inversion for 2-D crustal velocity structure, *Geophys. J. Int.,* **108,** 16–34.